

Full-dimensional three-state potential energy surfaces and state couplings for photodissociation of thiophenol

Linyao Zhang,^{a,b} Donald G. Truhlar,^{*b} and Shaozeng Sun^{*a}

^a School of Energy Science and Engineering,
Harbin Institute of Technology, Harbin 150001, P. R. China

^b Department of Chemistry, Chemical Theory Center, and Supercomputing Institute,
University of Minnesota, Minneapolis, Minnesota 55455, USA

Abstract

An analytic full-dimensional diabatic potential energy matrix (DPEM) for the lowest three singlet states of thiophenol (C₆H₅SH) at geometries accessible during photodissociation is constructed using the anchor points reactive potential (APRP) scheme. The data set used for modeling is obtained from electronic structure calculations including dynamic correlation via excitations into the virtual space of a three-state multi-configuration self-consistent field calculation. The resulting DPEM is a function of all the internal coordinates of thiophenol. The DPEM as a function of the S–H bond stretch and C–C–S–H torsion and the diabatic couplings along two in-plane bend modes and nine out-of-plane distortion modes are computed using extended multi-configurational quasi-degenerate perturbation theory followed by the fourfold way determination of diabatic molecular orbitals and model space diabatization by configurational uniformity, and this dependence of the DPEM is represented by general functional forms. Potentials along 31 tertiary internal degrees of freedom are modeled with system-dependent, primary-coordinate-dependent nonreactive molecular mechanics-type force fields that are parametrized by Cartesian Hessians calculated by generalized Kohn-Sham density functional theory. Adiabatic potential energy surfaces and nonadiabatic couplings are obtained by a transformation of the DPEM. The topography of the APRP PESs is characterized by vertical excitation energies, equilibrium geometries, vibrational frequencies, and conical intersections, and we find good agreement with available reference data. This analytic DPEM is suitable for full-dimensional electronically nonadiabatic molecular dynamics calculations of the photodissociation of thiophenol with analytic gradients in either the adiabatic or diabatic representation.

Emails: truhlar@umn.edu, sunsz@hit.edu.cn

I. Introduction

The concepts of adiabatic electronic states and adiabatic potential energy surfaces (PESs) are consequences of the Born-Oppenheimer (BO) separation.^{1,2} For molecular scattering, energy transfer processes, and chemical reactions that involve only a single electronic state, the BO separation has been enormously successful. Although the BO approximation was originally proposed for the ground electronic state, it is now common to use adiabatic electronic states as a basis for multi-state dynamics; this is sometimes called the generalized Born-Oppenheimer (GBO) approximation.³ Electronically nonadiabatic processes are important in photochemistry, photocatalysis, photovoltaics, transition metal chemistry, combustion chemistry, the atmosphere, surface chemistry, and a number of biological processes.^{4–14}

The adiabatic representation is uniquely defined by having a diagonal electronic Hamiltonian whose diagonal matrix elements (labeled as V_i) are the adiabatic PESs governing nuclear motion. For multi-state dynamics, one must also consider the couplings of the electronic states due to nuclear momentum and nuclear kinetic energy, and the associated matrix elements in the GBO are called nonadiabatic couplings (NACs); these couplings are usually small enough to be neglected when electronic states are well separated. However, nonadiabatic couplings usually become large and rapidly varying when the energies of two or more electronic states approach closely, and they become singular at conical intersections (CIs) where electronic states are degenerate. In general, conical intersections form a $(3N - 8)$ -dimensional seam in the $(3N - 6)$ -dimensional internal-coordinate space, where N is the number of atoms in the system. Nonadiabatic transitions occur most efficiently near conical intersection seams where nonadiabatic couplings cannot be neglected.^{15–25}

Whereas the GBO framework is based on coupled adiabatic states, electronically nonadiabatic processes may also be simulated in terms of a diabatic representation.²⁶ A diabatic representation is any representation in which the effect of the electronic state coupling due to the nuclear momentum and nuclear kinetic energy is negligible relative to the coupling by the electronic Hamiltonian; thus diabatic representations are not unique. (Strict diabatic states with

vanishing nuclear momentum couplings do not exist.²⁷⁾ In a diabatic representation, the electronic Hamiltonian matrix is not diagonal; we will call it the diabatic potential energy matrix (DPEM). The diagonal elements (labeled as U_{ii}) are the diabatic PESs (also called diabatic potentials), and the off-diagonal elements (labeled as U_{ij} with $i \neq j$) are called diabatic couplings.

To simulate the full dynamics of electronically nonadiabatic processes requires high-dimensional PESs and state couplings. Calculations with the full dimensionality, with the required ensemble averaging for comparison to experiment, and with high-accuracy electronic structure methods are usually affordable only if the PESs and couplings are fitted to analytic functions to avoid the cost of direct dynamics. It is impossible to fit the adiabatic PESs and couplings directly to an analytic form because the adiabatic PESs have cuspidal ridges at the $(3N - 8)$ -dimensional conical intersections, the NACs (which are the couplings in an adiabatic representation) are singular at these ridges, and one must also consider the geometric phase. In a diabatic representation, on the other hand, the PESs and couplings are smooth functions of nuclear coordinates, and there is no geometric phase. Therefore, our strategy is to fit a DPEM, but we note that once this is done the adiabatic PESs and couplings can be calculated by an inexpensive transformation from the diabatic fit so the dynamics may be carried out in either a diabatic or an adiabatic representation.

Photodissociation of thiophenol produces a phenylthiyl radical in which the singly occupied molecular orbitals (SOMOs) for the both the ground and first excited states are dominated by the occupied $3p$ orbital on sulfur. We use the notation n_σ and n_π to represent the nonbonding in-plane $3p$ orbital and out-of-plane $3p$ orbital, respectively. For thiophenol molecule, the $3p$ valence orbital of the sulfur is strongly delocalized and the out-of-plane $3p$ orbital contributes significantly to the π orbital that dominates the $S_0 \rightarrow S_2$ excitation, therefore we have chosen n_π to represent this π orbital and $n_\pi\sigma^*$ to represent $S_0 \rightarrow S_2$ excitation. This $n_\pi\sigma^*$ notation is also consistent with the labeling by Kim et al.²⁸

Photoinduced bond fission processes proceeding via an $n_\pi\sigma^*$ excited state are prototypes of electronically nonadiabatic reactions.^{29–37} The photodissociation of thiophenol is a

representative of these $n\pi^*$ -mediated reactions that has been extensively studied both experimentally and theoretically.^{28,38,39,40,41,42,43,44,45,46,47,48,49,50,51,52,53} The photo-induced S–H fission of thiophenol mainly involves the ground state and the first two excited singlet states (the participation of triplet states is uncertain but probably minor); these singlet states are labeled as $^1\pi\pi$, $^1\pi\pi^*$, and $^1n\pi\sigma^*$ in the diabatic representation and as S_0 , S_1 , and S_2 in the adiabatic representation. The $^1n\pi\sigma^*$ state is repulsive along the S–H dissociation coordinates and intersects the $^1\pi\pi^*$ and $^1\pi\pi$ states; the conical intersections are $(3N - 8)$ -dimensional subspaces of these $(3N - 7)$ -dimensional diabatic crossings. The resulting S_1 – S_2 and S_0 – S_1 conical intersections are labeled respectively as CI1 and CI2. Wave-packet simulations^{48,52} with reduced-dimensional PESs and couplings have been performed to investigate the photodissociation of thiophenol, but these 2D or 3D simulations only consider a few degrees of freedom and cannot explore how the other degrees of freedom are coupled to the bond fission process.

In the present study, we have constructed a set of full-dimensional potential energy surfaces and state couplings for thiophenol in the diabatic representation. The DPEMs are obtained by the orbital-dependent fourfold-way^{54,55,56} model-space⁵⁷ diabatization scheme that was applied to limited geometries of this system in a previous study,⁵³ and we fit them here using the anchor points reactive potential (APRP) scheme developed in our group.^{58,59,60,61} In the APRP method, the reactive degrees of freedom that are most relevant to the bond breaking (the S–H bond stretch and the C–C–S–H torsion) are fitted with general functional forms, and the other degrees of freedom are modeled with system-specific, geometry-specific, local, nonreactive molecular mechanics (MM) force fields. The resulting full-dimensional PESs and state couplings are functions of all 33 internal degrees of freedom of thiophenol.

The rest of this paper is arranged as follows. Section II describes the methods for the construction of PESs and state couplings. Section III presents the computations of system properties from the APRP PESs, in particular calculations of equilibrium geometries, excitation energies, vibrational frequencies, and conical intersections, and it compares these results with available experimental and high-level theoretical data. Section IV is a summary.

II. Methods and computational details

II.A. Anchor points reactive potential (APRP) method

The APRP scheme involves fitting the dependence of the potential on a few degrees of freedom to a general functional form and fitting the dependence on the other degrees of freedom to nonreactive molecular mechanics (MM) force fields. The latter degrees of freedom should only include those restricted (in the process to be studied) to small-amplitude vibrations or well-defined torsions. This method can be applied to either a single adiabatic PES⁵⁸ and or to a whole DPEM.^{59,60,61} Here we employ the latter. We will treat most of the modes as undergoing only small-amplitude vibrations or well-defined torsions during the photodissociation process, and this is justified in part by the experimental observation of the short S₁ excited state lifetime (~50 fs) of thiophenol.^{49,50}

The first step of the APRP scheme is to divide the internal coordinates into reactive coordinates (which include primary and, if any, secondary coordinates) and tertiary coordinates. The reactive coordinates are the ones that involve bond breaking or wide amplitude motion such that they cannot be accurately described by interpolation between geometry-dependent nonreactive MM force fields. The remaining coordinates are the tertiary coordinates. The reactive coordinates can be further divided into two subsets, the primary and secondary coordinates; the difference between the two subsets is how they are coupled to the tertiary coordinates. The coupling between the tertiary and primary coordinates can be strong, while the coupling between the secondary and tertiary coordinates should be insignificant. The DPEM matrix elements are written as

$$U_{ij}(\mathbf{q}, \mathbf{s}, \mathbf{Q}) = U_{ij}^{[1,2]}(\mathbf{q}, \mathbf{s}) + U_{ij}^{[3]}(\mathbf{Q}|\mathbf{q}) \quad (1)$$

where \mathbf{q} is the collection of primary coordinates; \mathbf{s} is the collection of secondary coordinates; \mathbf{Q} denotes the remaining internal coordinates that treated as tertiary coordinates; and the first and second terms on the right-hand-side are the reactive term and the tertiary term, respectively. In the current study, the first and second terms on the right-hand-side will be called reactive diabatic potentials and tertiary diabatic potentials, respectively, for the diagonal elements of the DPEM;

and they will be called reactive diabatic couplings and tertiary diabatic couplings, respectively, for the off-diagonal elements of the DPEM. The notation (\mathbf{q}, \mathbf{s}) denotes a functional dependence on \mathbf{q} and \mathbf{s} ; the notation $(\mathbf{Q}|\mathbf{q})$ denotes a functional dependence on \mathbf{Q} and a parametric dependence on \mathbf{q} .

Our treatment builds on previous applications of the APRP to similar problems.^{61,62,63} The reactive terms are fitted to general system-dependent functional forms with the tertiary coordinates frozen at the reactant ground state equilibrium geometry. Then we select a set of values of \mathbf{q}_a (with $a = 1, N_A$) called anchor points. At each \mathbf{q}_a we optimize the \mathbf{Q} to find a “constrained equilibrium” geometry for the each electronic state. Then we express each element of the DPEM for small-angle vibrations or torsions about the constrained equilibrium structure by using nonreactive molecular mechanics. The tertiary terms for each element of the DPEM are finally obtained as weighted linear combinations of these anchor-point fits.

II.B. Electronic structure calculations

All the data used in the fitting were obtained by electronic structure calculations. The potentials and couplings as functions of the primary coordinates and the diabatic couplings in the tertiary coordinates were obtained by extended multiconfigurational quasidegenerate perturbation theory (XMC-QDPT)^{64,65,66} followed by fourfold-way model-space diabaticization,^{54,55,56,57} with a minimally augmented-multiply polarized valence triple zeta (MG3S)⁶⁷ basis set. Technical details of the diabaticization methods (active orbitals, diabatic molecular orbitals, and diabatic prototypes et al.) can be found in our previous study.⁵³ These calculations were performed with the *GAMESS*^{68,69} electronic structure package.

The anchor-point geometry optimizations and Cartesian Hessian calculations for the construction of tertiary diabatic potentials were performed using Kohn-Sham density functional theory (KS-DFT)^{70,71} for the ground state and linear-response time dependent DFT (TDDFT)⁷² for excited states. We used the MN15⁷³ and τ -HCTHhyb⁷⁴ density functionals with the def-TZVP⁷⁵ basis set for the KS-DFT and TDDFT calculations, respectively. These calculations were performed using the *Gaussian 16*⁷⁶ electronic structure package.

II.C. Reactive coordinates

For photoinduced S–H fission of thiophenol, we have previously reported (without fitting) the diabatic and adiabatic potentials along the S–H bond stretch and C–C–S–H torsion, and both coordinates were shown to be important for the adiabatic-to-diabatic transformation.⁵³ However, the C–C–S–H torsion represents the orientation of the S–H bond well only when the benzene ring is planar. Following a similar treatment in a previous study on thioanisole,⁶⁰ we have chosen the S–H bond stretch (labeled as R) and an alternative angle labeled as ϕ to be the reactive coordinates. The angle ϕ is the average of two other angles, ϕ_1 and ϕ_2 , as illustrated in Fig. 1, where ϕ_1 is the angle between the C6–C2 vector and the projection of the S7–H13 vector onto the plane defined by the C6–C2 vector and the normal to the C6–C2–C1 plane; ϕ_2 is the angle between the C5–C3 vector and the projection of the S7–H13 vector on the plane defined by the C5–C3 vector and the normal to the C5–C3–C4 plane. Following the above definitions, the reactive coordinates are calculated as

$$R = |\mathbf{r}_{7-13}| \quad (2)$$

$$\phi = \frac{(|\phi_1| + |\phi_2|)}{2} \quad (3)$$

$$\cos \phi_1 = \frac{\mathbf{r}_{6-2} \cdot \mathbf{v}_{p1}}{|\mathbf{r}_{6-2}| |\mathbf{v}_{p1}|} \quad (4)$$

$$\cos \phi_2 = \frac{\mathbf{r}_{5-3} \cdot \mathbf{v}_{p2}}{|\mathbf{r}_{5-3}| |\mathbf{v}_{p2}|} \quad (5)$$

$$\mathbf{v}_{pi} = \mathbf{r}_{7-13} - \mathbf{v}_i \frac{\mathbf{v}_i \cdot \mathbf{r}_{7-13}}{|\mathbf{v}_i|^2}, \quad i = 1, 2 \quad (6)$$

$$\mathbf{v}_1 = \mathbf{r}_{6-2} \times (\mathbf{r}_{6-1} \times \mathbf{r}_{1-2}) \quad (7)$$

$$\mathbf{v}_2 = \mathbf{r}_{5-3} \times (\mathbf{r}_{5-4} \times \mathbf{r}_{4-3}) \quad (8)$$

where \mathbf{r}_{i-j} is the vector from atom i to atom j .

For modeling the diabatic potentials, R is treated as primary coordinate, and ϕ is treated as

secondary coordinate, but for the modeling of diabatic couplings, R and ϕ are both treated as primary coordinates. We can therefore write the following as a more specific version of eq. (1):

$$U_{ii}(R, \phi, \mathbf{Q}) = U_{ii}^{[1,2]}(R, \phi) + U_{ii}^{[3]}(\mathbf{Q}|R) \quad (9)$$

$$U_{ij}(R, \phi, \mathbf{Q}) = U_{ij}^{[1]}(R, \phi) + U_{ij}^{[3]}(\mathbf{Q}|R, \phi), \quad i \neq j \quad (10)$$

II.D. Construction of the diabatic potential energy matrix

II.D.1. Reactive diabatic potentials and reactive diabatic couplings

As mentioned above, the data used for modeling the reactive terms of the DPEM were calculated by XMC-QDPT/MG3S followed by fourfold way model-space diabatization (see Ref. 53 for details). These single-point calculations were performed within the (R, ϕ) -two-dimensional space with all the other coordinates fixed with their values at the ground-state equilibrium geometry. Then the diabatic potentials and couplings were fitted with selected analytic functions.

The potential of the diabatic $^1\pi\pi$ state (which is S_0 in the Franck-Condon region) is fitted using

$$U_{11}^{[1,2]}(R, \phi) = D_0 - D_1(1 + B_1(R - R_1))e^{(-B_1(R - R_1))} - \sum_{n=1}^3 D_{2n}e^{(-B_{2n}(R - R_{2n})^2)} \cos(2n\phi) \quad (11)$$

where D_0 , D_1 , B_1 , R_1 , D_{2n} , B_{2n} , and R_{2n} ($n = 1, 2, 3$) are parameters to be fitted, and where the D_1 term is a Rydberg⁷⁷ potential.

The potential of the diabatic $^1\pi\pi^*$ state (which is S_1 in the Franck-Condon region) is fitted using

$$U_{22}^{[1,2]}(R, \phi) = D_0 + D_1 \left(1 - e^{(-B_1(R - R_1))}\right)^2 - \sum_{n=1}^2 D_{2n}e^{(-B_{2n}(R - R_{2n})^2)} \cos(2n\phi) \quad (12)$$

where D_0 , D_1 , B_1 , R_1 , D_{2n} , B_{2n} , and R_{2n} ($n = 1, 2$) are parameters to be fitted, and where the D_1 term is a Morse⁷⁸ potential.

The potential of the diabatic $^1n\pi\sigma^*$ state (which is S_2 in the Franck-Condon region) is fitted

with eq. (11), the same functional form as used for the $^1\pi\pi$ state as these two diabatic states are similar in potential shape.

The symmetry of the diabatic couplings of thiophenol are the same as those of thioanisole (see Ref. 60 and its supporting information for more detail); in particular U_{12} is even and U_{13} and U_{23} are odd under reflection in the plane formed by the phenyl group. The following forms for the primary diabatic couplings are chosen to satisfy these symmetries for $\phi = n\pi/2$ (where $n = 0, 1, 2, 3, \dots$):

$$U_{12}^{[1]}(R, \phi) = \sum_{n=1}^2 D_n^{(12)} e^{\left(-B_n^{(12)} \left(R - R_n^{(12)}\right)^2\right)} \sin^2(2\phi) \quad (13)$$

$$U_{13}^{[1]}(R, \phi) = \sum_{n=1}^3 D_{2n}^{(13)} \operatorname{Re} \left(-B_{2n}^{(13)} \left(R - R_{2n}^{(13)}\right)^2 \right) \sin(2n\phi) \quad (14)$$

$$U_{23}^{[1]}(R, \phi) = \sum_{n=0}^2 D_{2n}^{(23)} e^{\left(-B_{2n}^{(23)} \left(R - R_{2n}^{(23)}\right)^2\right)} \sin(2^n \phi) \quad (15)$$

where $D_k^{(ij)}$, $B_k^{(ij)}$, and $R_k^{(ij)}$ ($i, j = 1, 2, 3$, and k is an integer) are parameters to be fitted.

II.D.2. Tertiary diabatic potentials

The tertiary diabatic potentials are calculated using the following form,

$$U_{ii}^{[3]}(\mathbf{Q}|R) = \sum_{a=1}^{N_A} U_{ii}^{[3](a)}(\mathbf{Q}) T^{(a)}(R) \quad (16)$$

where $U_{ii}^{[3](a)}(\mathbf{Q})$ are the MM-like potentials with specific parameters at each anchor point a ; and $T^{(a)}(r)$ are tent functions that specify the weight of each anchor point during the interpolation, as given by

$$T^{(1)}(R) = \begin{cases} 1 & R < R_1 \\ \frac{(R-R_2)^4}{(R-R_2)^4 + (R-R_1)^4} & R_1 \leq R < R_2 \\ 0 & \text{otherwise} \end{cases} \quad (17)$$

$$T^{(a)}(R) = \begin{cases} \frac{(R-R_{a-1})^4}{(R-R_a)^4 + (R-R_{a-1})^4} & R_{a-1} \leq R < R_a \\ \frac{(R-R_{a+1})^4}{(R-R_{a+1})^4 + (R-R_a)^4} & R_a \leq R < R_{a+1} \\ 0 & \text{otherwise} \end{cases} \quad (18)$$

for $a = 2, 3, \dots, N_A - 1$

$$T^{(N_A)}(R) = \begin{cases} \frac{(R-R_{N_A-1})^4}{(R-R_{N_A})^4 + (R-R_{N_A-1})^4} & R_{N_A-1} \leq R < R_{N_A} \\ 1 & R > R_{N_A} \\ 0 & \text{otherwise} \end{cases} \quad (19)$$

where R_a is the value of coordinate R at anchor point a , and the order of the anchor points is arranged with ascending R_a ; N_A is the last anchor point.

As mentioned above, the tertiary diabatic potentials $U_{ii}^{[3](a)}(\mathbf{Q})$ are modeled by a nonreactive force field at each anchor point (for $a = 1, 2, \dots, N_A$). The parameters of these force fields are optimized so as to reproduce the Cartesian Hessian matrix of each anchor point geometry which has been partially optimized by DFT or TDDFT. Although the tertiary space could in principle be modeled by 31 nonredundant coordinates (thiophenol has 33 internal coordinates, and 2 of them are in the reactive coordinate space), in this application we actually use redundant internal coordinates for each $U_{ii}^{[3](a)}(\mathbf{Q})$. All the coordinates and their corresponding types are listed in Table I with the connectivity and numbering of the atoms shown in Fig. 1. The force field formula can then be written as composition of different contributions based on the type of coordinates as follows,

$$U_{ii}^{[3](a)} = U_{\text{rel},ii}^a + U_{ii}^{\text{S},a} + U_{ii}^{\text{B},a} + U_{ii}^{\text{T},a} + U_{ii}^{\text{D},a} \quad (20)$$

where $U_{\text{rel},ii}^a$ is the energy of state i at the constrained equilibrium geometry with primary and secondary coordinates fixed at the corresponding anchor point, relative to the energy of the reference geometry; the last four terms on the right-hand-side are harmonic bond stretches $U_{ii}^{\text{S},a}$, valence angle bends $U_{ii}^{\text{B},a}$, cosine torsions $U_{ii}^{\text{T},a}$, and harmonic out-of-plane distances $U_{ii}^{\text{D},a}$ which are given by the following forms,

$$U_{ii}^{\text{S},a} = \frac{1}{2} \sum_n k_{n,ii}^{\text{S},a} \left(\frac{R_n - R_{0,n,ii}^a}{R_n} \right)^2 \quad (21)$$

$$U_{ii}^{\text{B},a} = \frac{1}{2} \sum_n k_{n,ii}^{\text{B},a} \left(\cos \delta_n - \cos \delta_{0,n,ii}^a \right)^2 \quad (22)$$

$$U_{ii}^{\text{T},a} = \frac{1}{2} \sum_n k_{n,ii}^{\text{T},a} \left(1 - \cos \left[m_n \left(\tau_n - \tau_{0,n,ii}^a \right) \right] \right)^2 \quad (23)$$

$$U_{ii}^{\text{D},a} = \frac{1}{2} \sum_n k_{n,ii}^{\text{D},a} \left(d_n - d_{0,n,ii}^a \right)^2 \quad (24)$$

where the sums are over all tertiary coordinates of the given type; the k parameters are force constants; the subscript $(0,n,ii)$ represents the equilibrium value of that term for coordinate n ; the m_n parameters in eq. (23) are dihedral multiplicities. Note that there are no cross terms coupling different tertiary coordinates in the current study; although the neglect of cross term cannot be justified if one uses Cartesian coordinates, it is a good approximation when one uses internal coordinates.⁷⁹

To determine the MM parameters, we first need to specify the anchor points, which for the tertiary diabatic potentials are simply specified by the value of R . The anchor points are chosen to include the regions of the ground-state equilibrium ($R = 1.34$ Å), the first conical intersection (CI1 with $R \approx 1.4$ Å), the second conical intersection (CI2 with $R \approx 2.7$ Å), and the asymptotic limit. We used seven anchor points with $R = 1.20, 1.35, 1.60, 2.10, 2.50, 3.40$, and 5.00 Å for

$U_{11}^{[3]}$ (the ${}^1\pi\pi$ potential), three anchor points with $R=1.25, 1.35$, and 1.60 Å for $U_{22}^{[3]}$ (the ${}^1n\pi\sigma^*$ potential), and seven anchor points with $R = 1.25, 1.35, 1.60, 2.10, 2.50, 3.40$, and 5.00 Å for $U_{33}^{[3]}$ (the ${}^1\pi\pi^*$ potential). For most anchor points, the MM potential is expressed in terms of 61 redundant internal coordinates; However, the last anchor point represents the asymptotic limit with Hessian matrix calculated from optimized thiophenoxy radical, so only 60 internal coordinates are used at the last anchor point (the C–S–H bend δ_{31} no longer exists in the radical). The anchor point geometries are obtained by constrained geometry optimizations at each R for each state. All the anchor point geometries are planar with $\phi = 0^\circ$ and C_s . The constrained geometry optimizations and Cartesian Hessian calculations are performed with DFT for the ground state and with TDDFT for the excited state (the functionals used are τ -HCTHhyb for anchor points with $R = 3.40$ and 5.00 Å and MN15 for anchor points with other R values; the def-TZVP basis set is used for all of these calculations).

The next step is MM parameter optimization for each anchor point, and this is performed with our modified version⁸⁰ of the *QuickFF*⁸¹ package. We assume the tertiary diabatic potentials are equal to the tertiary adiabatic potentials, which is justified by the fact that the tertiary coordinates are largely spectator coordinates. With this assumption, we use Cartesian Hessians of the adiabatic states to calculate the MM parameters for modeling the tertiary diabatic potentials. The input information needed by *QuickFF* consists of the anchor point geometry (obtained by the constrained optimization), the corresponding Cartesian Hessian matrix, the pre-defined internal coordinates listed in Table I, and the selected functional forms in eqs. (21)–(24). The force field parameters are then optimized to minimize the error between the force field and *ab initio* Cartesian Hessian. The details of this kind of calculation can be found in the Ref. 81. The main change we made in the *QuickFF* package is that we replaced the simple quadratic functions (eq. (2.6) and (2.7) in Ref. 81) with our more globally valid functions (eq. (21) and (22)) for bond stretches and angle bends.

II.D.3. Tertiary diabatic couplings

The tertiary diabatic couplings are constructed in a different way than the tertiary diabatic

potentials. The first difference, as mentioned above, is that for the diabatic couplings we treat both reactive coordinates, R and ϕ , as primary coordinates. Therefore we need a product of tent functions to interpolate, and the tertiary couplings are written as,

$$U_{ij}^{[3]}(\mathbf{Q}|R, \phi) = s_{ij}(\phi) \sum_{a=1}^2 \sum_{b=1}^3 U_{ij}^{[3](a,b)}(\mathbf{Q}) T^{(a)}(R) T^{(b)}(-\cos 2\phi) \quad (25)$$

where tent functions $T^{(a)}(R)$ are for the interpolation along R ; and tent functions $T^{(b)}(-\cos 2\phi)$ are used for the interpolation along ϕ . The argument of the latter tent function is chosen because it increases monotonically for $0 \leq \phi \leq \pi/2$ and give the correct periodicity along ϕ . The factor $s_{ij}(\phi)$ is used to enforce the correct parity of the tertiary couplings and the overall diabatic couplings U_{ij} (U_{12} is even, and U_{13} and U_{23} are odd about $\phi = n\pi/2$, where $n = 0, 1, 2, 3, \dots$, as discussed in Section C.1 and Ref. 60):

$$s_{12}(\phi) = 1$$

$$s_{13}(\phi) = s_{23}(\phi) = \begin{cases} 1, & \sin 2\phi > 0 \\ 0, & \sin 2\phi = 0 \\ -1, & \sin 2\phi < 0 \end{cases} \quad (26)$$

A second important difference from the treatment of the diabatic potentials is that for modeling the tertiary diabatic couplings, we use a subset of the 33 nonredundant internal coordinates, and in particular, following our previous work on phenol⁵⁹ and thioanisole,⁶⁰ only internal angular coordinates are employed for this part of the potential. The selection of which coordinates to use was based on examination of the changes of the couplings along each of the angular coordinates (valence bends, dihedral torsions, and out-of-plane bends). As a result, we selected two in-plane bends (denoted Q_1 and Q_2) and nine out-of-plane distortion coordinates (denoted Q_3 to Q_{11}), and their definitions are listed in Table II. Then

$$U_{ij}^{[3](a,b)}(\mathbf{Q}) = \sum_{n=1}^{11} U_{ij,n}^{[3](a,b)}(Q_n) \quad (27)$$

where

$$U_{ij,n}^{[3](a,b)}(Q_n) = \left[K_{1,n,ij}^{(a,b)}(Q_n - Q_{0,n}) + K_{2,n,ij}^{(a,b)}(Q_n - Q_{0,n})^2 \right] \exp\left(\frac{-(Q_n - Q_{0,n})^2}{\sigma^2} \right) \quad (28)$$

where the parameters $K_{1,n,ij}^{(a,b)}$, and $K_{2,n,ij}^{(a,b)}$ are the force constants to be fitted; and $Q_{0,n}$ denotes the value at the ground-state equilibrium geometry. (Notice that although we use the state-specific origins of the Taylor series for the tertiary diabatic potentials, we take $Q_{0,n}$ to be independent of state index i for the tertiary couplings.) The Gaussian function is used to damp the polynomial for large $(Q_n - Q_{0,n})$ to avoid unphysical results for large deviations from the reference geometries, and the parameter σ is set to the large value of 50° so as not to unduly disrupt the Taylor series in its region of validity.

To determine the force constants in Eq. (28), we first need to specify anchor point locations. Three R values (1.45, 2.90, and 4.00 Å) and five ϕ values (0° , 30° , 50° , 70° , and 90°) are chosen; therefore we have 15 anchor points for the modeling of tertiary diabatic couplings. The first two R values are near CI1 and CI2, respectively, where the state couplings are most significant. The last R value is used to decay the tertiary diabatic couplings to zero in the asymptotic region, and this is achieved by setting all force constants in eq. (28) equal to zero when $R = 4.00$ Å. For each of the remaining 10 anchor points, 6 distorted geometries are generated for each of the 11 internal coordinates (Q_1 to Q_{11}) listed in Table II by displacing corresponding coordinate at values of -30° , -20° , -10° , 10° , 20° , 30° . The diabatic couplings of the distorted geometries (660 in total) are then obtained in the same way as for the reactive diabatic couplings (by performing XMC-QDPT calculations followed by fourfold way and model space diabatization). Finally, the force constants are obtained through one-dimensional fitting to *ab initio* data for each coupling (U_{12} , U_{13} , and U_{23}) for each selected internal coordinate at each selected anchor point.

II.D.4. Gradients, adiabatic potentials, and nonadiabatic couplings

The adiabatic potential energies are obtained from the diagonalization of the diabatic matrix,

$$\mathbf{V} = \mathbf{C}^{-1}\mathbf{U}\mathbf{C}, \quad (29)$$

where \mathbf{V} is diagonal, and \mathbf{C} is the orthogonal matrix with elements U_{ij} that diagonalizes the DPEM. The Cartesian components of the adiabatic gradients and nonadiabatic couplings are given by⁸²

$$\frac{\partial V_i}{\partial x_\alpha} = \sum_j \sum_k C_{ji} \frac{\partial U_{jk}}{\partial x_\alpha} C_{ki} \quad (30)$$

$$F_{ij,\alpha} = \hbar \left\langle \psi_i \left| \frac{\partial}{\partial x_\alpha} \right| \psi_j \right\rangle = \begin{cases} \frac{1}{V_j - V_i} \sum_k \sum_l C_{ki} \frac{\partial U_{kl}}{\partial x_\alpha} C_{lj} & (i \neq j) \\ 0 & (i = j) \end{cases} \quad (31)$$

where x_α denotes a Cartesian coordinate. As described above, all elements of the diabatic matrix are fitted with respect to internal coordinates; the transformation of the internal-coordinate partial derivatives to Cartesian gradients as needed in eqs. (30) and (31) is performed by the chain rule and the Wilson \mathbf{B} matrix.⁸³

$$\frac{\partial U_{ij}}{\partial x_\alpha} = \sum_n \frac{\partial U_{ij}}{\partial q_n} \frac{\partial q_n}{\partial x_\alpha} \quad (32)$$

where q_n is an internal coordinate, and $\partial q_n / \partial x_\alpha$ is obtained from the Wilson \mathbf{B} matrix.

II.E. Fortran routines

A Fortran subroutine with all optimized parameters is provided in the Supporting Information and also available in the POTLIB library. The subroutine can provide the DPEM and the adiabatic potential energy surfaces, their analytic gradients, and the nonadiabatic couplings.

II.F. Additional computational details

The geometry optimization and vibrational analysis with the fitted APRP PESs were performed using *Polyrate*⁸⁴ software package. The minimum energy conical intersections (MECIs) between adiabatic state i and adiabatic state j were calculated by minimizing a penalty function

$$\frac{(V_i + V_j)}{2} + \alpha(V_i - V_j)^2 \quad (33)$$

using a BFGS⁸⁵ optimizer, where V_i and V_j are adiabatic energies and $\alpha = 10^5 E_h^{-2}$. We have run thousands of trajectories with the coupled APRP PESs using the *ANT*⁸⁶ software package to make sure that the total energy and angular momentum are conserved and that trajectories do not visit regions that give unphysical results.

II.G. Excitation energies

We calculate three kinds of excitation energies. The vertical excitation energy (VEE) is the potential energy difference calculated at the ground state equilibrium geometry. The adiabatic excitation energy is defined as the potential energy difference of $^1\pi\pi^*$ and $^1\pi\pi$ states, with each at its own equilibrium geometry. The 0–0 excitation energy is the adiabatic energy plus the harmonic zero-point vibrational energy difference of $^1\pi\pi^*$ and $^1\pi\pi$ states. We do not calculate adiabatic or 0–0 excitation energies for the $^1\pi\pi$ - $^1n\pi\sigma^*$ excitation because the $^1n\pi\sigma^*$ state of thiophenol is repulsive and does not have a minimum in the Franck-Condon region.

III. Results and discussion

III.A. Vertical excitation energies

The vertical excitation energies (VEEs) of thiophenol and thiophenoxyl radical as well as the S–H bond dissociation energies (BDEs) as calculated from the APRP PESs and various electronic structure methods are listed in Table III. For the $^1\pi\pi$ - $^1\pi\pi^*$ excitation, we also present the adiabatic and 0–0 excitation energies; these are in Table IV.

Table III shows that the vertical excitation energies predicted by the APRP PESs are in good agreement with the XMC-QDPT/MG3S values that were used to generate the data used for the fit. This is especially significant since first the XMC-QDPT adiabatic energies were converted to diabatic energies, then they were fit in the diabatic representation, and then the diabatic fit was converted to adiabatic energies for this comparison.

The APRP vertical excitation energies also agree well with our best estimates given by completely renormalized equation-of-motion coupled cluster theory with singles, doubles, and

noniterative connected triples (CR-EOM-CCSD(T))^{87,88} with aug-cc-pV(T+d)Z basis set^{89,90,91,92} and by XMC-QDPT/aug-cc-pV(T+d)Z.

The S–H bond dissociation energy to the \tilde{X}^2B_1 state of thiophenoxyl and the vertical excitation energy of thiophenoxyl radical that given by the APRP PESs also agree well with the XMC-QDPT/MG3S and best estimate values.

The adiabatic and 0–0 excitation energies calculated from APRP PESs compare quite well with XMC-QDPT and experimental^{43,49} results (with small deviation of ~ 0.06 eV), as shown in Table IV.

III.B. Equilibrium geometries and frequencies

Geometry optimizations with our fitted APRP PESs result in planar equilibrium structures with C_s symmetry for both the ground ($^1\pi\pi$, S_0 in Franck-Condon region) and the first excited ($^1\pi\pi^*$, S_1 in Franck-Condon region) state of thiophenol. For the $^1\pi\pi$ state, bond lengths and bond angles obtained from the APRP PES, from microwave spectroscopy,⁹³ and from DFT calculations with the M06-2X⁹⁴ functional are compared in Table V. The APRP geometric parameters are in quite good agreement with experimental and DFT results, with deviations for all bond lengths less than 0.02 Å and deviations for most bond angles less than 0.7°. The C1–S7–H13 APRP bond angle shows a relatively large deviation (1.6° from the experiment and 2.2° from M06-2X). This large deviation is understandable since geometric parameters are not explicitly used in the fit, and the C1–S7–H13 bond angle is treated as a tertiary coordinate.

Although the $^1\pi\pi^*$ state of thiophenol is bound in the Franck-Condon region, the $^1\pi\pi^*$ vibronic bands are hard to identify in the electronic spectrum.⁴⁷ In our study, we identified an equilibrium structure for the $^1\pi\pi^*$ state by CASSCF/MG3S calculations, and it is quite similar to the ground state equilibrium geometry. However, similarly to our group's previous finding for thioanisole, unconstrained TDDFT calculations with various functionals (MN15, τ -HCTHhyb, and B3LYP^{95,96,97,98}) and basis sets (MG3S, aug-cc-pVTZ, and def2-TZVP⁹⁹) failed to locate an equilibrium structure for the $^1\pi\pi^*$ state in the Franck-Condon region.

Figure 2 shows qualitative agreement between the ground-state harmonic vibrational

frequencies of thiophenol calculated from the fit and experimental frequencies. The mean and median unsigned percentage differences are 7.0% and 4.6% respectively, and 26 out of 33 frequencies are reproduced within 10%.

III.C. Selected cuts of adiabatic and diabatic potentials and nonadiabatic and diabatic couplings

Next we compare the diabatic potential energy surfaces (Fig. 3), diabatic couplings (Fig. 4a, Fig. 4b), norms of nonadiabatic couplings (Fig. 4c, Fig. 4d) and adiabatic potential energy surfaces (Fig. 5) given by XMC-QDPT/MG3S (when available) and APRP PESs as functions of R for selected values of ϕ with other coordinates fixed at the ground-state equilibrium geometry. As shown in these figures, the results given by our APRP PESs agree well the XMC-QDPT results along the reactive coordinates. The diabatic couplings U_{13} (Fig. 4a) has a noticeable error for $R < 1.3$ Å and $\phi = 30^\circ$, however, the widely separated diabatic potential energies U_{11} and U_{33} at this region mean that the deviations in the diabatic couplings in this region do not have a large impact on adiabatic energies, as can be seen from the adiabatic energy curves for $\phi = 30^\circ$ shown in Fig. 5b. The bump in diabatic couplings U_{13} and U_{23} between $R = 2.2$ and 2.5 Å, which can be seen in Fig. 4a and Fig. 4b, is due to the crossing of the third adiabatic state ($^1\pi\pi^*$ diabatic state) with a higher non-considered state and thus the bump is ignored during the fitting. This is a common problem in fitting diabats whose diagonalization reproduces the diabats, namely that the highest-energy considered adiabatic state often has an crossing or locally avoided crossing with the first omitted adiabatic state; this occurs at high energy and should not have a big effect on the dynamics. The direct calculation of nonadiabatic coupling with XMC-QDPT is not affordable currently, especially with the large active space and basis set used here; therefore the present method of diabaticizing the XMC-QDPT results and calculating the NACs from the diabatic-to-adiabatic transformation is way to produce NACs that are not affordable by direct calculation. As can be seen in Fig. 4c and Fig. 4d, our APRP PESs give quite reasonable nonadiabatic couplings from the diabatic-to-adiabatic transformation.

Next we test the quality of the APRP PESs for predicting the surfaces beyond the training

data. The diabatic potential energy curves along R with C–S–H bond angle (θ_{CSH} , which is a tertiary coordinate) at four values that not at the equilibrium value (which is 96.7° for the ground state) and with other coordinates fixed at values of ground state equilibrium parameters are shown in Fig. 6. The errors become larger when θ_{CSH} deviates more from the equilibrium value; nevertheless, our fit is still in an acceptable range for $\theta_{\text{CSH}} = 80$ - 110° .

To further check the performance of our APRP PESs for arbitrarily distorted geometries during trajectory calculations, we randomly selected some points along two trajectories that cover important reaction regions. We again get satisfactory results, as can be seen in Fig. 7 which compares the adiabatic energies for these arbitrary points as given by APRP PESs and XMC-QDPT/MG3S.

Three-dimensional plots of diabatic and adiabatic energies as function of R and ϕ are shown in Fig. 8. The diabatic crossing seams, which correspond to the hypersurfaces where $U_{22} = U_{33}$, $U_{11} = U_{33}$, and $U_{11} = U_{22}$ are illustrated in Fig. 8a by projection onto the (R, ϕ) two-dimensional plane. The crossing seams show where the diabatic states change their order.

III.D. Conical intersections

The conical intersections are $(3N - 8)$ -dimensional seams, where N is the number of atoms of the molecule. It is difficult to locate conical intersection seams directly by using electronic structure calculations, but it can be done more easily with the analytic full-dimensional PESs such as we have here. The S_1 - S_2 minimum-energy conical intersection (MECI1) and the S_0 - S_1 minimum-energy conical intersection (MECI2) obtained with our fitted APRP PESs are both in C_s symmetry, with R equal to 1.44 \AA and 2.69 \AA , respectively, see Table VII.

It is also possible to map out one-dimensional conical intersection cuts along some paths with fitted analytic PESs on hand. We select two paths to illustrate the S_1 - S_2 intersection (CI1) and the S_0 - S_1 intersection (CI2). Path 1 is obtained by minimizing eq. (33) with R fixed at selected values and the other coordinates relaxed. Path 2 is obtained by minimizing eq. (33) with the torsion angle $\tau_{2-1-7-13}$ fixed at selected values, with bond lengths r_{1-2} and r_{1-7} and bond angle θ_{2-1-7} fixed at equilibrium values, and with other coordinates relaxed. Four one-dimensional

conical intersection cuts are obtained with these two paths computed for each of the CI1 and CI2 seams; the cuts are plotted against selected R and $\tau_{2-1-7-13}$ values as shown in Fig. 9 and the XMC-QDPT/MG3S energies for each APRP CI point are also given for comparison. It can be seen clearly from Fig. 9 that the adiabatic energies of the two degenerate states increase when a conical intersection seam moves away from the corresponding MECI. Nevertheless, the fact that, as shown in Fig. 9, the XMC-QDPT states are nearly degenerate where the APRP states are degenerate is very encouraging. Table S1 to Table S4 of the Supporting Information list the adiabatic energies (used in Fig. 9) given by APRP PESs and by XMC-QDPT/MG3S and some geometric parameters along these four conical intersection cuts. The mean unsigned deviations of the APRP energies from the XMC-QDPT results for these CI geometries are 0.06 eV, 0.15 eV, and 0.10 eV for S_0 , S_1 , and S_2 , respectively, with maximum deviation of ~ 0.32 eV for a significantly distorted geometry with $\tau_{2-1-7-13} = 20^\circ$. Here it should be kept in mind that the locations of the CI seams are quite sensitive to the potential energies; therefore it is not unexpected that potential energies yielded by the APRP PESs are not precisely degenerate where the XMC-QDPT ones are, and vice versa. In this light, the general nature of the results in Fig. 7 is quite encouraging.

IV. Summary

High-dimensional potential energy surfaces and state couplings are very useful for studying electronically nonadiabatic processes, but conventional fitting methods cannot fit high-dimensional surfaces or surfaces with conical intersections. In the present work, we have constructed full-dimensional three-state analytic potential energy surfaces and state couplings with analytic gradients for thiophenol using the APRP scheme. The vertical excitation energies, equilibrium geometries, and vibrational frequencies obtained from the APRP PESs agree well with the available reference data. The fitted APRP PESs cover all degrees of freedom for a wide range of geometries from the Frank-Condon region to the dissociation limit of the S–H bond. (The surfaces and couplings are full-dimensional but are only designed to be accurate for geometries accessible during photolysis of the S–H bond; thus they might be called semiglobal

full-dimensional surfaces and couplings.) The potential energies given by our APRP PESs for random selected geometries from test trajectories agree well with high-level XMC-QDPT calculations, which means our fits can give accurate results for geometries beyond the training data and can be used to study the photodissociation of thiophenol to elucidate the role of internal motions in this photo-induced electronically nonadiabatic reaction.

Supplementary material

Equilibrium geometries, energies, and frequencies obtained from APRP PESs are available. Geometries, and energies of conical intersections obtained from APRP PESs are given. A Fortran routine for DPEM, adiabatic PESs and corresponding gradients is also provided. The Fortran subroutine is also available from the online POTLIB library at <https://comp.chem.umn.edu/potlib/>.

Acknowledgments

This work was supported in part by the U. S. Department of Energy, Office of Basic Energy Sciences, under grant no. DE-SC0015997, by National Natural Science Foundation of China (No. 51536002), and Linyao Zhang was also supported by a scholarship from China Scholarship Council (201706120185).

Table I. Coordinates used for modeling tertiary diabatic potentials^a

Coordinates	Type	Definition
R_1 to R_6	bond stretch	C–C
R_7 to R_{11}		C–H
R_{12}		C–S
δ_{13} to δ_{18}	valence bend	C–C–C
δ_{19} to δ_{28}		C–C–H
δ_{29} to δ_{30}		C–C–S
δ_{31}^b		C–S–H
τ_{32} to τ_{37}		C–C–C–C
τ_{38} to τ_{47}	torsion	C–C–C–H
τ_{48} to τ_{49}		C–C–C–S
τ_{50} to τ_{53}		H–C–C–H
τ_{54} to τ_{55}		H–C–C–S
d_{56} to d_{61}	out-of-plane distance ^c	S7–C6–C2–C1
		H8–C1–C3–C2
		H9–C2–C4–C3
		H10–C3–C5–C4
		H11–C4–C6–C5
		H12–C5–C1–C6

^aThe connectivity and numbering of atoms are based on Fig. 1.

^bInternal coordinate δ_{31} is not used for the anchor point with $R = 5\text{\AA}$.

^cOut-of-plane distance $a-b-c-d$ denotes the distance from atom d to the $a-b-c$ plane.

Table II. Internal coordinates (S_1 to S_{11}) used for modeling tertiary diabatic couplings^a

Coordinates	Definition
δ_1	S7–C1–C2 bend
δ_2	S7–C1–C6 bend
τ_1	C6–C1–C2–C3 torsion
τ_2	C1–C2–C3–C4 torsion
τ_3	C2–C3–C4–C5 torsion
τ_4	C3–C4–C5–C6 torsion
τ_5	C4–C5–C6–C1 torsion
τ_6	C5–C6–C1–C2 torsion
Q_1	$2^{-1/2} (\delta_1 - \delta_2)$
Q_2	H13–S7–C1 bend
Q_3	$6^{-1/2} (\tau_1 - \tau_2 + \tau_3 - \tau_4 + \tau_5 - \tau_6)$
Q_4	$12^{-1/2} (-\tau_1 + 2\tau_2 - \tau_3 - \tau_4 + 2\tau_5 - \tau_6)$
Q_5	$4^{-1/2} (\tau_1 - \tau_3 + \tau_4 - \tau_6)$
Q_6	S7 out-of-plane bend
Q_7	H8 out-of-plane bend
Q_8	H9 out-of-plane bend
Q_9	H10 out-of-plane bend
Q_{10}	H11 out-of-plane bend
Q_{11}	H12 out-of-plane bend

^aSee Fig. 1 for atomic numbering.

Table III. Gas-phase vertical excitation energies (VEEs) of thiophenol (PhSH) and thiophenoxyl (PhS*) and the S–H bond dissociation energy (BDE) to the \tilde{X}^2B_1 state of the thiophenoxyl radical (in eV)^{a,b}

Method	PhSH			PhS*
	$^1\pi\pi^* - ^1\pi\pi$	$^1n\pi\sigma^* - ^1\pi\pi$	BDE	$\tilde{A}^2B_2 - \tilde{X}^2B_1$
APRP	4.61	4.95	3.55	0.32
XMC-QDPT/MG3S	4.62	5.07	3.51	0.27
XMC-QDPT/aug-cc-pV(T+d)Z	4.58	5.03	3.60	0.27
EOM-CCSD/aug-cc-pV(T+d)Z	4.89	5.15	3.66	0.35
CR-EOM-CCSD(T)/aug-cc-pV(T+d)Z	4.57	4.95	3.66	0.19
TD-MN15/MG3S	4.95	5.00	3.65	0.10
TD-B3LYP/MG3S	4.76	5.15	3.63	0.39
TDA- τ -HCTHhyb/def-TZVP	4.79	5.07	3.63	0.41

^aVertical excitation energies are calculated at the S_0 equilibrium geometry optimized by M06-2X/aug-cc-pVTZ, unless for APRP. For APRP they are calculated at the S_0 equilibrium geometry optimized on the APRP ground-state adiabatic potential energy surface.

^bAbbreviations: XMC-QDPT: extended multi-configuration quasidegenerate perturbation theory; EOM-CCSD: equation-of-motion coupled cluster theory with single and double; CR-EOM-CCSD(T): completely renormalized EOM-CCSD with quasiperturbative connected triple excitations; TD: time-dependent density functional theory with the linear response approximation; TDA: time-dependent density functional theory with the Tamm–Dancoff approximation; MN15, B3LYP, and τ -HCTHhyb: exchange-correlation functionals; MG3S, aug-cc-pV(T+d)Z, def-TZVP: basis sets. See Ref. 53 for details about methods and basis sets not described in the present paper.

Table IV. Adiabatic and 0–0 excitation energies (in eV) for ${}^1\pi\pi\text{--}{}^1\pi\pi^*$ excitation of thiophenol^a

	Adiabatic	0–0
APRP	4.44	4.29
XMC-QDPT/MG3S//CASSCF/MG3S	4.41	4.28
Exp.	not available	4.27 ^b /4.34 ^c

^aSee Section II.G for the definition of adiabatic and 0–0 excitation energies.

^bFrom Ref. 43

^cFrom Ref. 49

Table V. Geometric parameters of the S_0 equilibrium geometry of thiophenol^a

	APRP	M06-2X ^b	Microwave ^c
Bond lengths (Å)			
C1–C2	1.395	1.391	
C2–C3	1.388	1.387	
C3–C4	1.391	1.387	
C4–C5	1.390	1.388	
C5–C6	1.389	1.386	
C6–C1	1.393	1.392	
C–C (average)	1.391	1.389	1.396
C1–S7	1.771	1.769	1.773
S7–H13	1.353	1.338	1.333
C–H (average)	1.083	1.082	1.080 (Fixed)
Bond angles (deg.)			
C1–C2–C3	120.1	120.0	
C2–C3–C4	120.5	120.5	
C3–C4–C5	119.3	119.4	120 (Fixed)
C4–C5–C6	120.5	120.5	
C5–C6–C1	120.0	120.1	
C6–C1–C2	119.6	119.6	120 (Fixed)
C1–S7–H13	94.5	96.7	96.1

^aSee Fig. 1 for atomic numbering.

^bBasis set: aug-cc-pVTZ.

^cFrom Ref. 39, “fixed” means these values are fixed during fitting procedure.

Table VI. Geometric parameters of the S_1 equilibrium geometry of thiophenol^a

	APRP	MN15 ^b
Bond lengths (Å)		
C1–C2	1.412	1.413
C2–C3	1.426	1.423
C3–C4	1.407	1.405
C4–C5	1.407	1.406
C5–C6	1.425	1.422
C6–C1	1.414	1.408
C–C (average)	1.415	1.413
C1–S7	1.724	1.704
S7–H13	1.311	1.336
C–H (average)	1.082	1.084
Bond angles (deg.)		
C1–C2–C3	117.7	117.1
C2–C3–C4	118.6	118.9
C3–C4–C5	123.2	123.4
C4–C5–C6	119.0	118.4
C5–C6–C1	117.3	117.7
C6–C1–C2	124.1	124.4
C1–S7–H13	94.3	97.6

^aSee Fig. 1 for atomic numbering.

^bBasis set: aug-cc-pVTZ. Imaginary frequency of $341i$ cm^{-1} is present for the C–C–S–H torsional mode.

Table VII Adiabatic energies (in eV) and geometric parameters given by APRP and XMC-QDPT at some key geometries^a

Geometry	APRP			XMC-QDPT/MG3S			R	ϕ (deg.)	S_1^b (deg.)	S_2^b (deg.)
	V_1	V_2	V_3	V_1	V_2	V_3				
S_0 equilibrium	0.00	4.61	4.95	0.05	4.65	5.01	1.353	0.0	-3.4	94.5
S_1 equilibrium	0.16	4.44	5.21	0.22	4.47	5.25	1.311	0.0	-3.3	94.3
MECI1	0.14	4.68	4.68	0.23	4.62	4.70	1.441	0.0	-4.2	90.9
MECI2	3.39	3.39	6.35	3.39	3.55	6.26	2.690	0.0	-0.9	104.6

^aEnergies are relative to V_1 at the S_0 equilibrium geometry given by the APRP surface.

^bSee Table II for the definition of coordinates S_1 and S_2 .

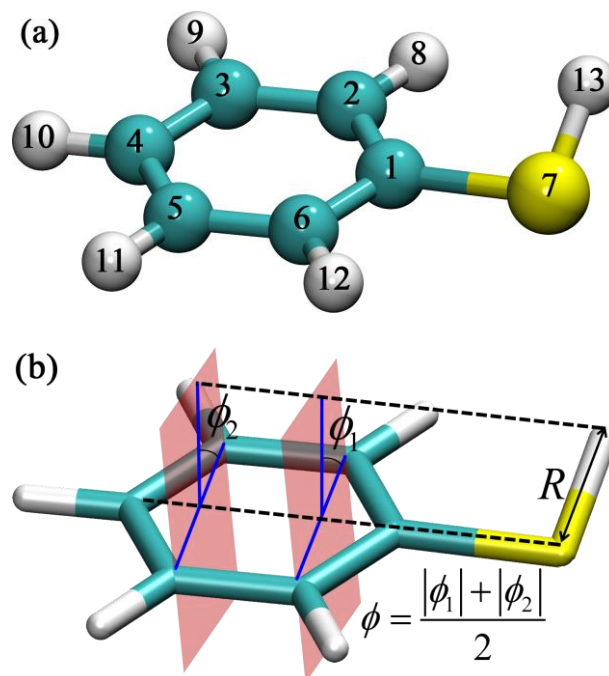


Fig. 1. (a) Numbering of atoms. (b) Definition of coordinates R and ϕ ; the pink plane used for defining ϕ_1 contains C2 and C6 and is normal to the C2-C1-C6 plane; the pink plane used for defining ϕ_2 contains C3 and C5 and is normal to the C3-C4-C5 plane (see the text for more detail).

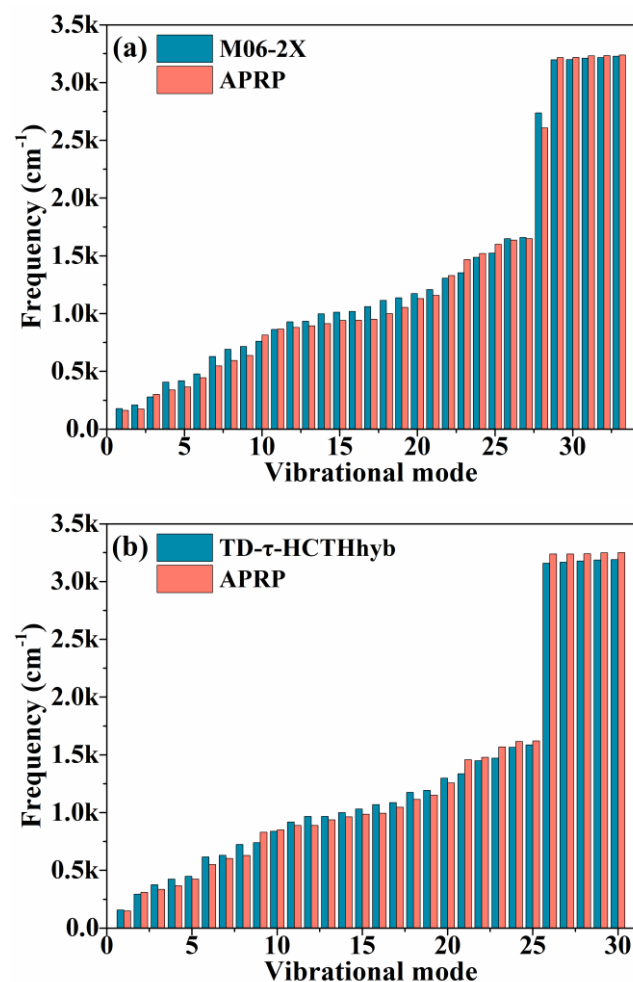


Fig. 2. Ground state frequencies of (a) thiophenol and (b) thiophenoxyl radical as calculated by APRP surfaces and by M06-2X/aug-cc-pVTZ for S_0 and TD- τ -HCTHhyb/def-TZVP for S_1

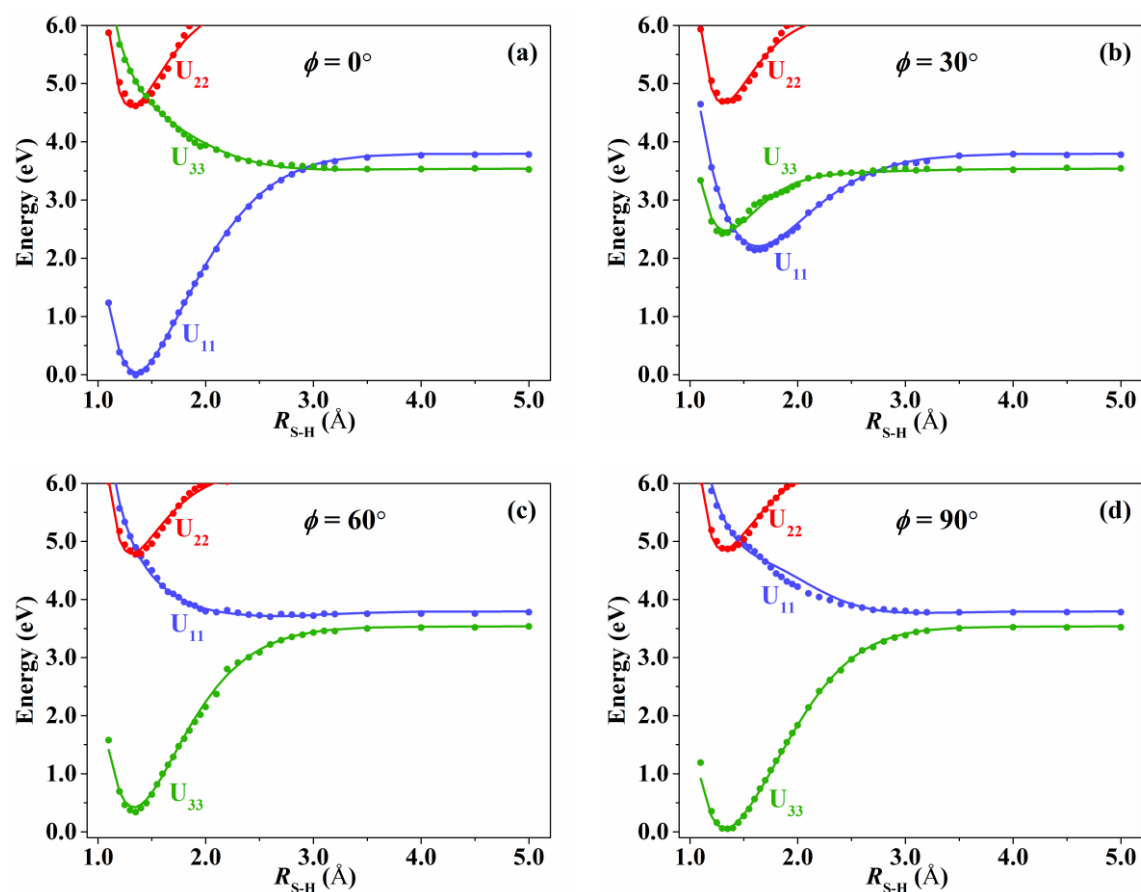


Fig. 3. APRP (solid lines) and XMC-QDPT/MG3S (dots) diabatic energies along R for different values of ϕ with other internal coordinates fixed at the S_0 equilibrium geometry. (a) $\phi = 0^\circ$. (b) $\phi = 30^\circ$. (c) $\phi = 60^\circ$. (d) $\phi = 90^\circ$.

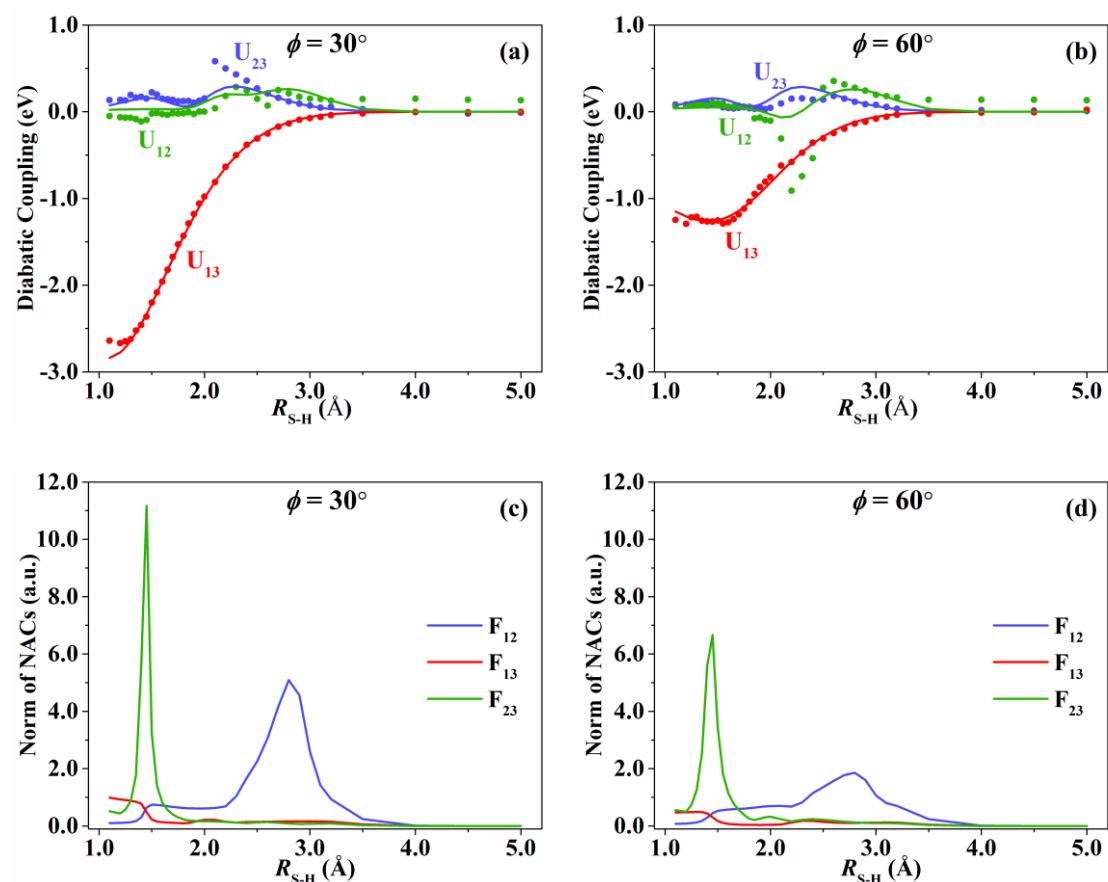


Fig. 4. APRP (solid lines) and XMC-QDPT/MG3S (dots, when available) diabatic couplings and norm of the nonadiabatic couplings along R for two different values of ϕ with other internal coordinates fixed at the S_0 equilibrium geometry. (a) diabatic coupling, $\phi = 30^\circ$. (b) diabatic coupling, $\phi = 60^\circ$. (c) magnitude of nonadiabatic coupling vector, $\phi = 30^\circ$. (d) magnitude of nonadiabatic coupling vector, $\phi = 60^\circ$.

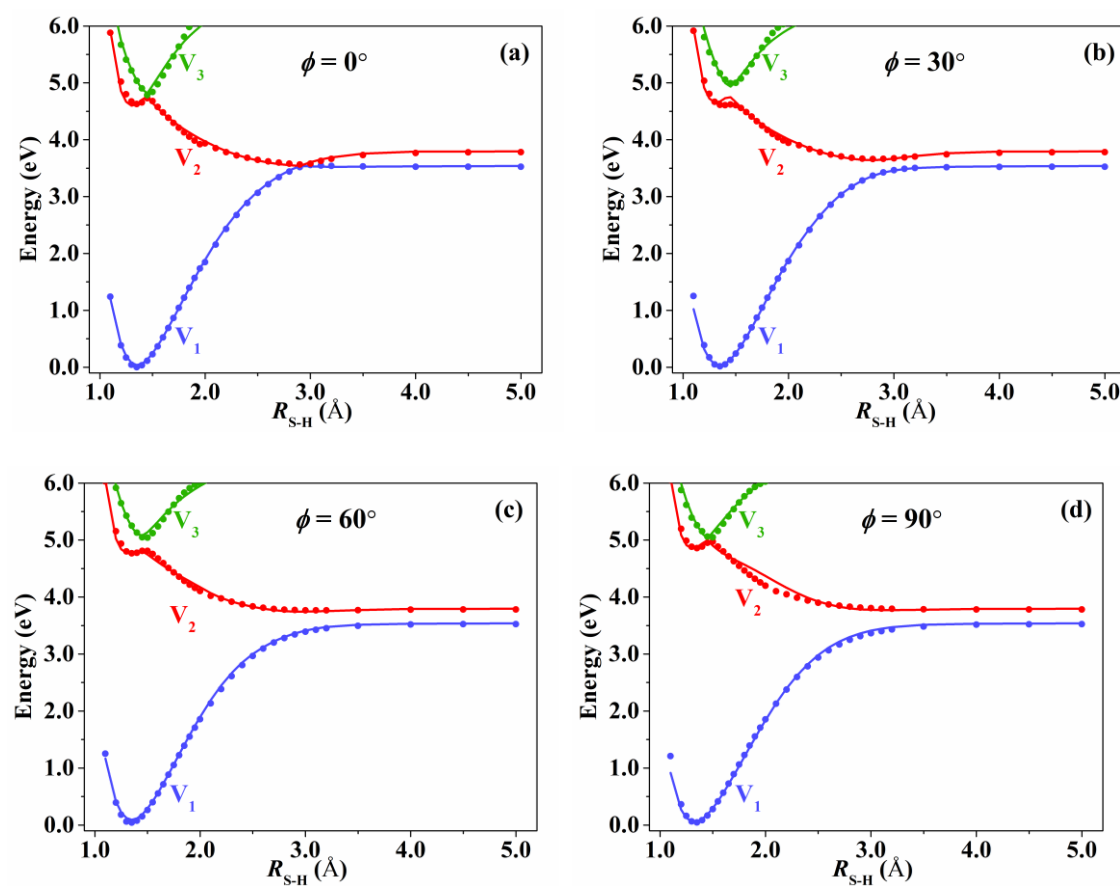


Fig. 5. APRP (solid lines) and XMC-QDPT/MG3S (dots) adiabatic energies along R for different values of ϕ with other internal coordinates fixed at the S_0 equilibrium geometry. (a) $\phi = 0^\circ$. (b) $\phi = 30^\circ$. (c) $\phi = 60^\circ$. (d) $\phi = 90^\circ$.

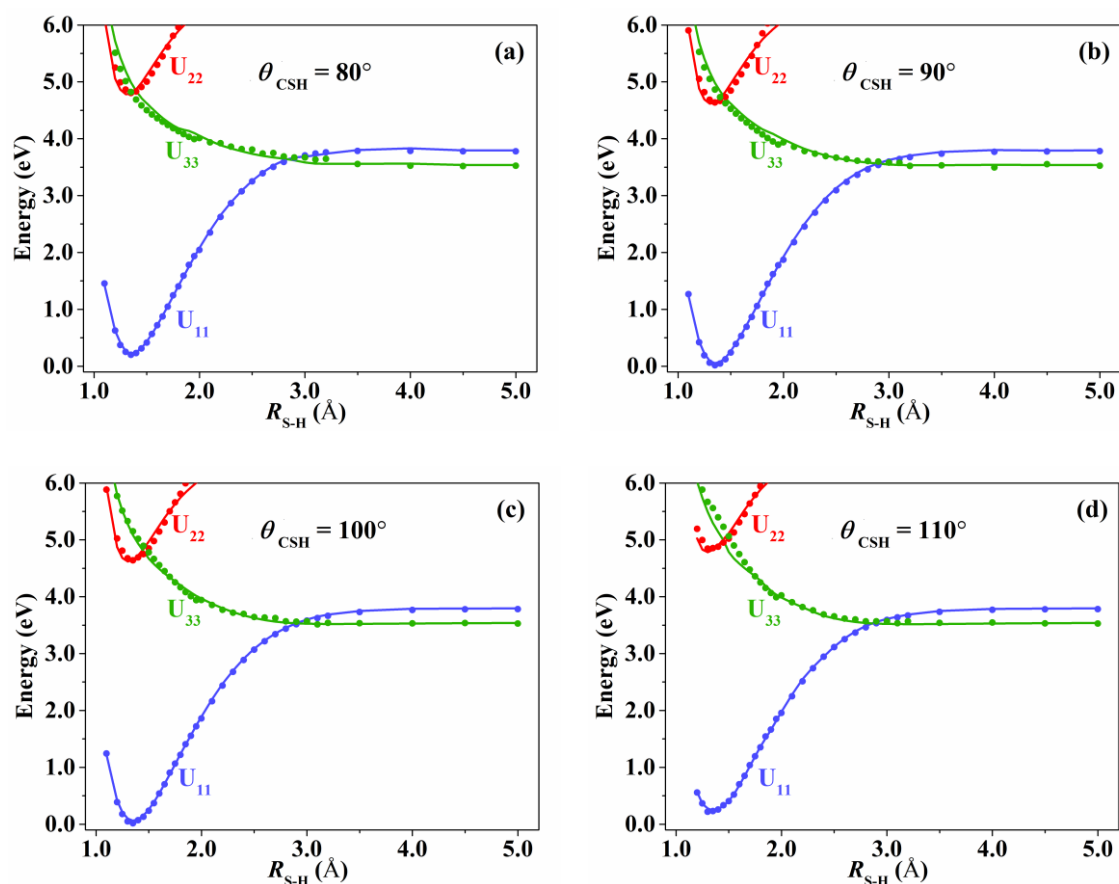


Fig. 6. APRP (solid lines) and XMC-QDPT/MG3S (dots) diabatic energies along R for two C-S-H bend angles not equal to its value for S_0 equilibrium geometry. The other internal coordinates are fixed at the S_0 equilibrium geometry. (a) $\phi = 80^\circ$. (b) $\phi = 90^\circ$. (c) $\phi = 100^\circ$. (d) $\phi = 110^\circ$.

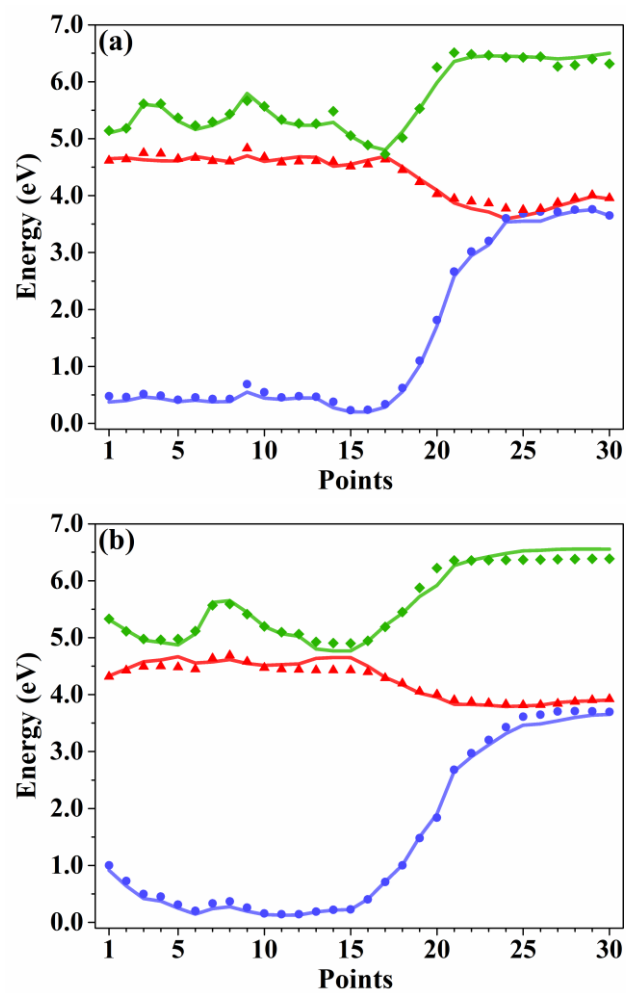


Fig. 7. APRP (solid lines) and XMC-QDPT/MG3S (dots) adiabatic energies along two randomly selected trajectories. (a) first trajectory. (b) second trajectory.

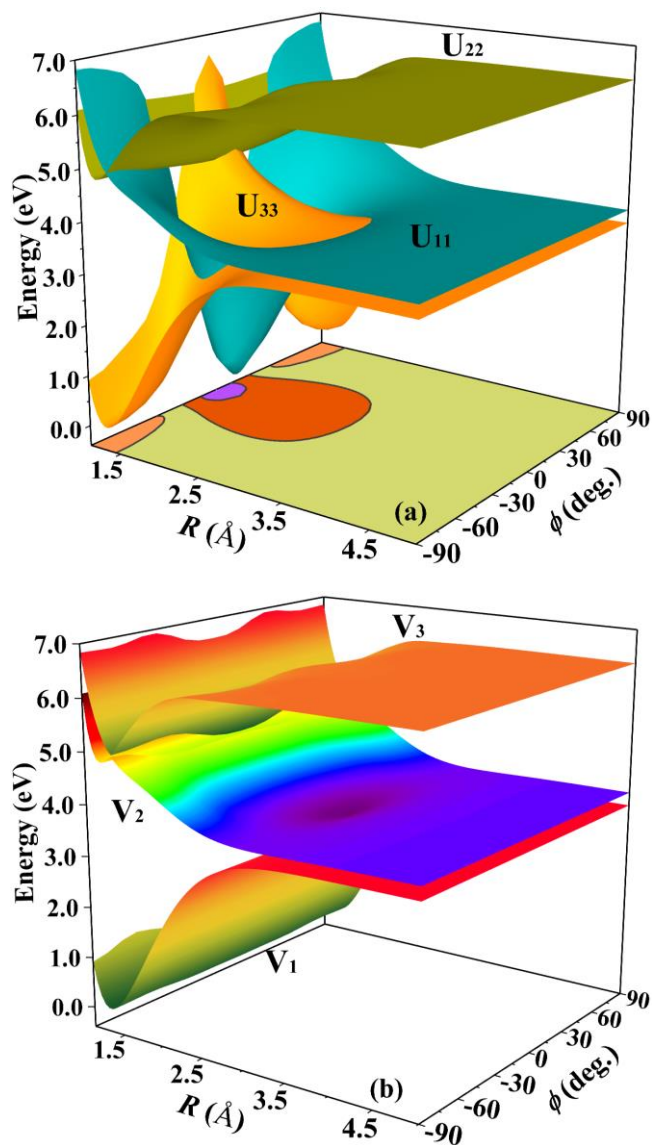


Fig. 8 Three-dimensional plot of APRP diabatic energies with projected diabatic crossing seams (a) and adiabatic energies (b) along R and ϕ with other coordinates fixed at values of ground state equilibrium geometry.

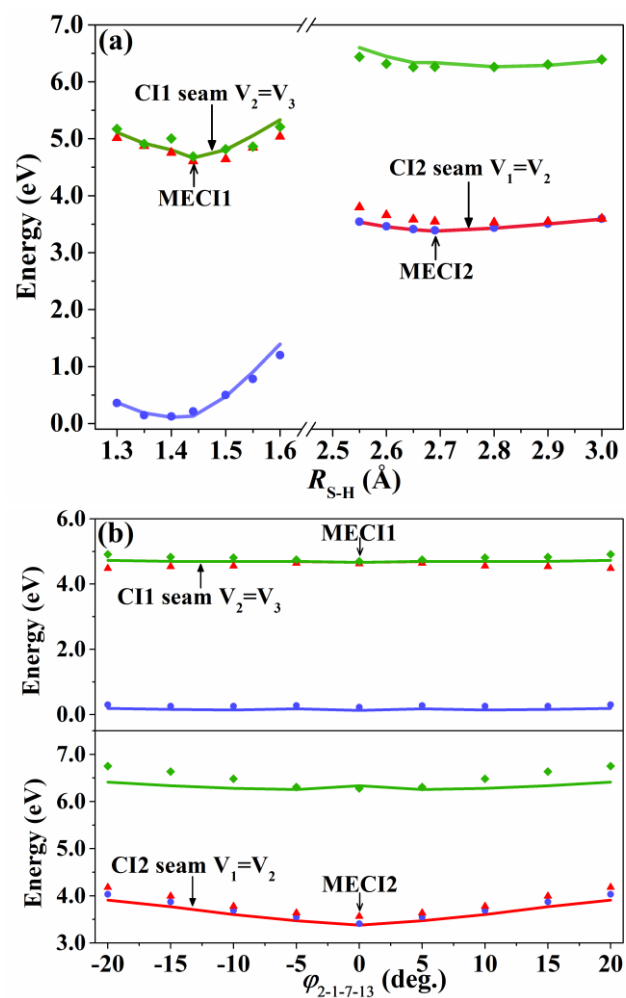


Fig. 9 One-dimensional conical intersection cuts along (a) path 1 and (b) path 2 as given by APRP PESs (solid lines) and XMC-QDPT/MG3S (dots).

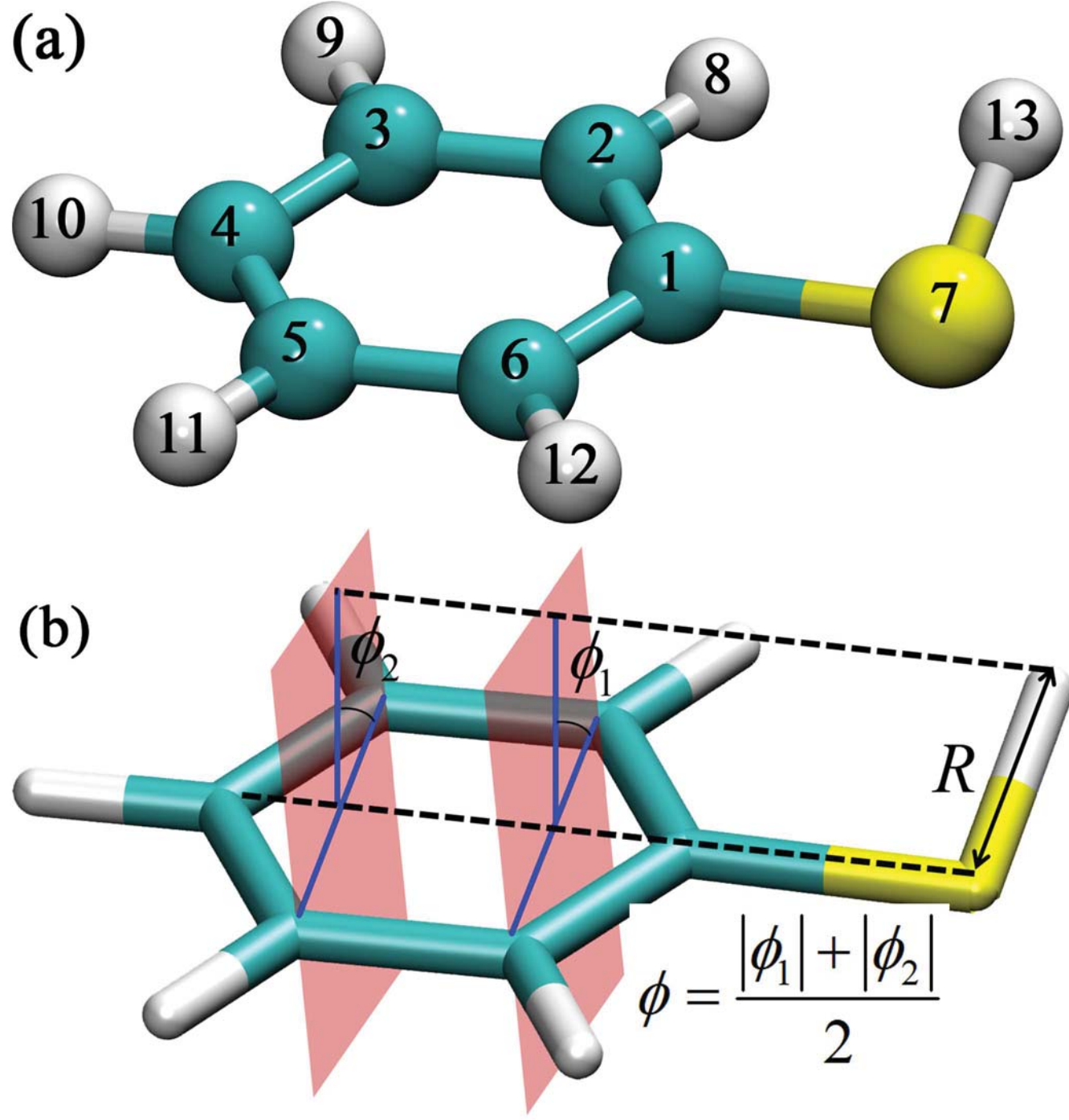
References

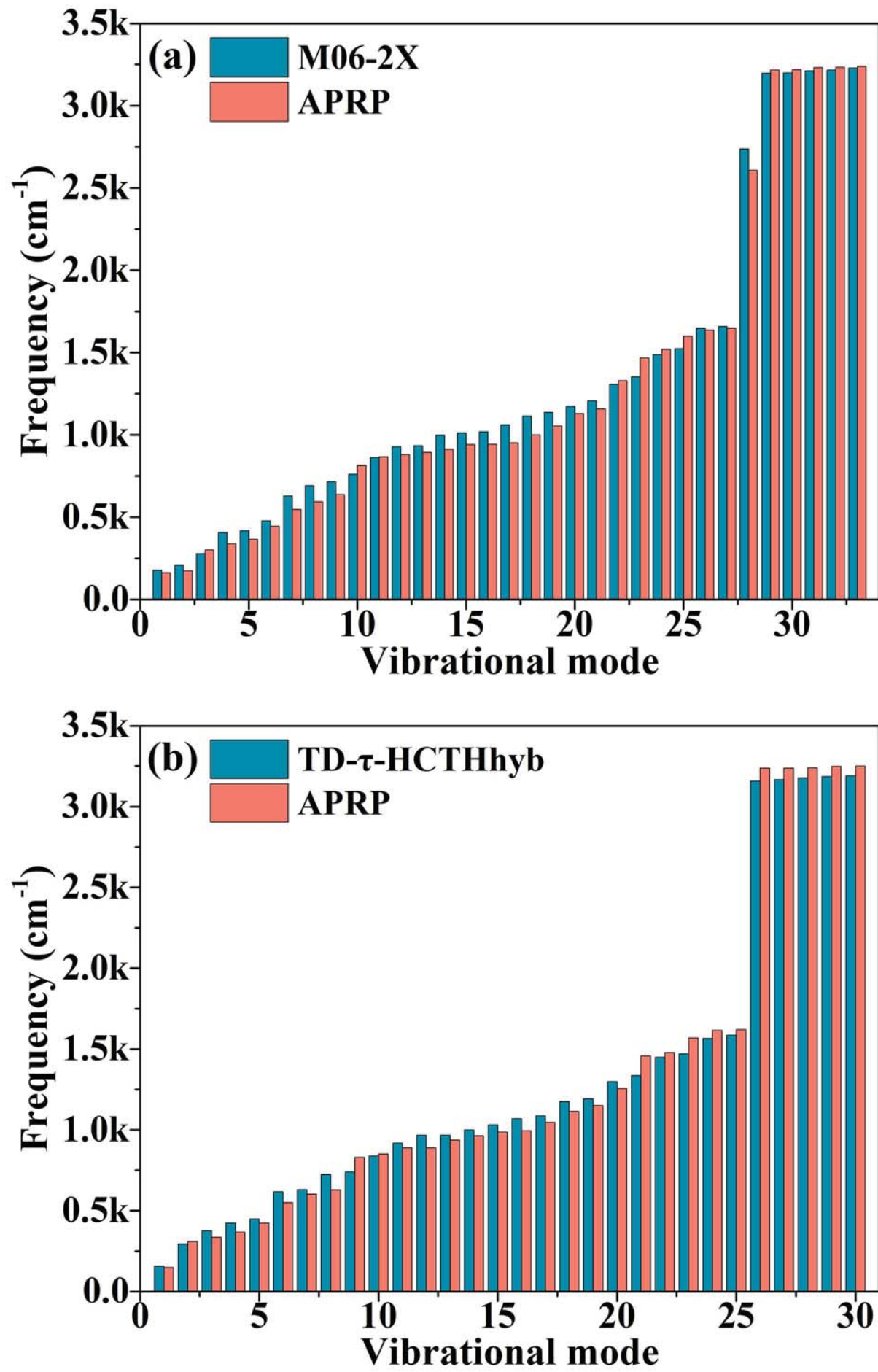
- ¹ M. Born and R. Oppenheimer, *Ann. Phys.* **84**, 457 (1927).
- ² D. G. Truhlar, in *Encyclopedia of Physical Science and Technology*, 3rd Edition, edited by R. A. Meyers (Academic Press, New York, 2003), pp. 9.
- ³ A. W. Jasper, B. K. Kendrick, C. A. Mead, and D. G. Truhlar, in *Modern Trends in Chemical Reaction Dynamics: Experiment and Theory (Part I)*, edited by X. Yang and K. Liu (World Scientific, River Edge, NJ, 2004), pp. 329-391.
- ⁴ M. L. Hernández, J. M. Alvariño, A. Laganà, M. Rosi, A. Sgamellotti, *Int. J. Quantum Chem.* **86**, 79 (2002).
- ⁵ D. Polli, P. Altoè, O. Weingart, K. M. Spillane, C. Manzoni, D. Brida, G. Tomasello, G. Orlandi, P. Kukura, and R. A. Mathies, *Nature* **467**, 440 (2010).
- ⁶ G. Zgrablic, A. M. Novello, and F. Parmigiani, *J. Am. Chem. Soc.* **134**, 955 (2011).
- ⁷ D. R. Yarkony, *Chem. Rev.* **112**, 481 (2011).
- ⁸ J. C. Tully, *J. Chem. Phys.* **137**, 22A (2012).
- ⁹ F. Plasser, M. Barbatti, A. J. A. Aquino, and H. Lischka, *Theor. Chem. Acc.* **131**, 1 (2012).
- ¹⁰ A. W. Jasper and R. Dawes, *J. Chem. Phys.* **138**, 154313 (2013).
- ¹¹ V. Balzani, P. Ceroni, and A. Juris, *Photochemistry and Photophysics* (Wiley-VCH, Weinheim, 2014).
- ¹² E. Brunk and U. Rothlisberger, *Chem. Rev.* **115**, 6217 (2015).
- ¹³ A. M. Wodtke, *Chem. Soc. Rev.* **45**, 3641 (2016).
- ¹⁴ W. Li, R. Long, J. Tang, and O. V. Prezhdo, *J. Phys. Chem. Lett.* **10**, 3788 (2019).
- ¹⁵ E. Teller, *J. Phys. Chem.* **41**, 109 (1937).
- ¹⁶ W. Kauzmann, *Quantum Chemistry* (Academic Press, New York, 1957), p. 696.
- ¹⁷ E. Teller, *Isr. J. Chem.* **7**, 287 (1969).
- ¹⁸ M. D. Hack and D. G. Truhlar, *J. Chem. Phys.* **110**, 4315 (1999).
- ¹⁹ A. Köhl and W. Domcke, *Chem. Phys.* **259**, 227 (2000).
- ²⁰ M. Ben-Nun and T. J. Martinez, *Chem. Phys.* **259**, 237 (2000).
- ²¹ S. Zilberg and Y. Haas, *Chem. Phys.* **259**, 249 (2000).
- ²² S. Matsika and P. Krause, *Annu. Rev. Phys. Chem.* **62**, 621 (2011).
- ²³ *Conical Intersections: Theory, Computation, and Experiment*, edited by W. Domcke, D. R. Yarkony, and H. Köppel (World Scientific, Hackensack, New York, 2011).
- ²⁴ W. Domcke and D. R. Yarkony, *Annu. Rev. Phys. Chem.* **63**, 325 (2012).
- ²⁵ M. S. Schuurman and A. Stolow, *Annu. Rev. Phys. Chem.* **69**, 427 (2018).
- ²⁶ A. W. Jasper, C. Zhu, S. Nangia, and D. G. Truhlar, *Faraday Discuss.* **127**, 1 (2004).
- ²⁷ C. A. Mead and D. G. Truhlar, *J. Chem. Phys.* **77**, 6090 (1982).
- ²⁸ I. S. Lim, J. S. Lim, Y. S. Lee, and S. K. Kim, *J. Chem. Phys.* **126**, 34306 (2007).
- ²⁹ A. L. Sobolewski and W. Domcke, *Chem. Phys. Lett.* **315**, 293 (1999).
- ³⁰ A. L. Sobolewski and W. Domcke, *Chem. Phys.* **259**, 181 (2000).
- ³¹ A. L. Sobolewski and W. Domcke, *J. Phys. Chem. A* **105**, 9275 (2001).

- ³² A. L. Sobolewski, W. Domcke, C. Dedonder-Lardeux, and C. Jouvet, *Phys. Chem. Chem. Phys.* **4**, 1093 (2002).
- ³³ M. N. R. Ashfold, B. Cronin, A. L. Devine, R. N. Dixon, and M. G. D. Nix, *Science* **312**, 1637 (2006).
- ³⁴ M. N. R. Ashfold, G. A. King, D. Murdock, M. G. D. Nix, T. A. A. Oliver, and A. G. Sage, *Phys. Chem. Chem. Phys.* **12**, 1218 (2010).
- ³⁵ G. A. King, T. A. A. Oliver, and M. N. R. Ashfold, *J. Chem. Phys.* **132**, 214307 (2010).
- ³⁶ G. M. Roberts, D. J. Hadden, L. t. Bergendahl, A. M. Wenge, S. J. Harris, T. N. V. Karsili, M. N. R. Ashfold, M. J. Paterson, and V. G. Stavros, *Chem. Sci.* **4**, 993 (2013).
- ³⁷ X. Xu, K. R. Yang, and D. G. Truhlar, *J. Chem. Theory Comput.* **9**, 3612 (2013).
- ³⁸ J. S. Lim, I. S. Lim, K. Lee, D. Ahn, Y. S. Lee, and S. K. Kim, *Angew. Chem. Int. Ed.* **45**, 6290 (2006).
- ³⁹ A. L. Devine, M. G. D. Nix, R. N. Dixon, and M. N. R. Ashfold, *J. Phys. Chem. A* **112**, 9563 (2008).
- ⁴⁰ M. N. R. Ashfold, A. L. Devine, R. N. Dixon, G. A. King, M. G. D. Nix, and T. A. A. Oliver, *Proc. Natl. Acad. Sci. U.S.A.* **105**, 12701 (2008).
- ⁴¹ J. S. Lim, Y. S. Lee, and S. K. Kim, *Angew. Chem. Int. Ed.* **47**, 1853 (2008).
- ⁴² J. S. Lim, H. Choi, I. S. Lim, S. B. Park, Y. S. Lee, and S. K. Kim, *J. Phys. Chem. A* **113**, 10410 (2009).
- ⁴³ T. A. A. Oliver, Y. Zhang, M. N. R. Ashfold, and S. E. Bradforth, *Faraday Discuss.* **150**, 439 (2011).
- ⁴⁴ T. S. Venkatesan, S. G. Ramesh, Z. Lan, and W. Domcke, *J. Chem. Phys.* **136**, 174312 (2012).
- ⁴⁵ T. A. A. Oliver, G. A. King, D. P. Tew, R. N. Dixon, and M. N. R. Ashfold, *J. Phys. Chem. A* **116**, 12444 (2012).
- ⁴⁶ Y. Zhang, T. A. A. Oliver, M. N. R. Ashfold, and S. E. Bradforth, *Faraday Discuss.* **157**, 141 (2012).
- ⁴⁷ H. Choi, Y. C. Park, Y. S. Lee, H. An, and K. K. Baek, *Chem. Phys. Lett.* **580**, 32 (2013).
- ⁴⁸ H. An, H. Choi, Y. S. Lee, and K. K. Baek, *ChemPhysChem* **16**, 1529 (2015).
- ⁴⁹ H. S. You, S. Han, J. S. Lim, and S. K. Kim, *J. Phys. Chem. Lett.* **6**, 3202 (2015).
- ⁵⁰ V. Ovejas, M. Fernández-Fernández, R. Montero, and A. Longarte, *Chem. Phys. Lett.* **661**, 206 (2016).
- ⁵¹ G.-S.-M. Lin, C. Xie, and D. Xie, *J. Phys. Chem. A* **121**, 8432 (2017).
- ⁵² G.-S.-M. Lin, C. Xie, and D. Xie, *J. Phys. Chem. A* **122**, 5375 (2018).
- ⁵³ L. Zhang, D. G. Truhlar, and S. Sun, *Phys. Chem. Chem. Phys.* **20**, 28144 (2018).
- ⁵⁴ H. Nakamura and D. G. Truhlar, *J. Chem. Phys.* **115**, 10353 (2001).
- ⁵⁵ H. Nakamura and D. G. Truhlar, *J. Chem. Phys.* **117**, 5576 (2002).
- ⁵⁶ H. Nakamura and D. G. Truhlar, *J. Chem. Phys.* **118**, 6816 (2003).
- ⁵⁷ S. L. Li, D. G. Truhlar, M. W. Schmidt, and M. S. Gordon, *J. Chem. Phys.* **142**, 64106 (2015).
- ⁵⁸ K. R. Yang, X. Xu, and D. G. Truhlar, *J. Chem. Theory Comput.* **10**, 924 (2014).
- ⁵⁹ K. R. Yang, X. Xu, J. Zheng, and D. G. Truhlar, *Chem. Sci.* **5**, 4661 (2014).
- ⁶⁰ S. L. Li and D. G. Truhlar, *J. Chem. Phys.* **146**, 64301 (2017).
- ⁶¹ Y. Shu and D. G. Truhlar, *Chem. Phys.* (2018).
- ⁶² X. Xu, J. Zheng, K. R. Yang, and D. G. Truhlar, *J. Am. Chem. Soc.* **136**, 16378 (2014).
- ⁶³ S. L. Li and D. G. Truhlar, *J. Chem. Phys.* **147**, 44311 (2017).

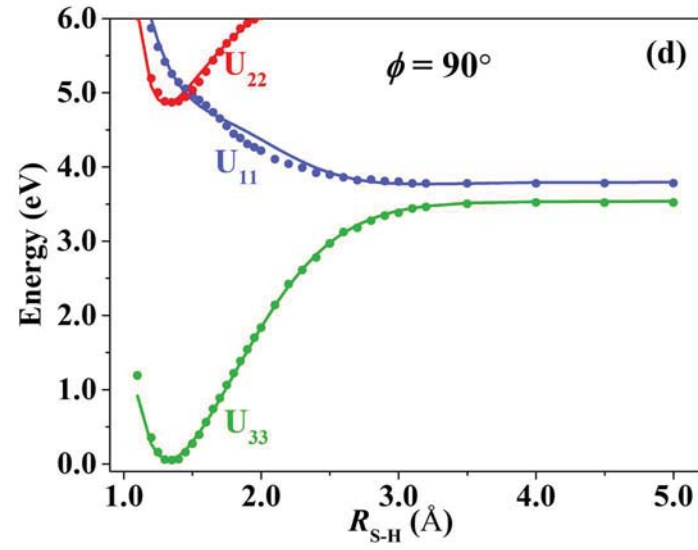
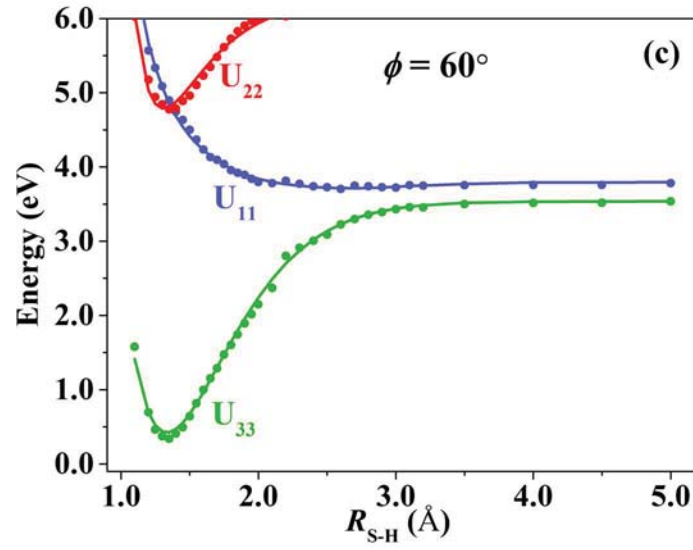
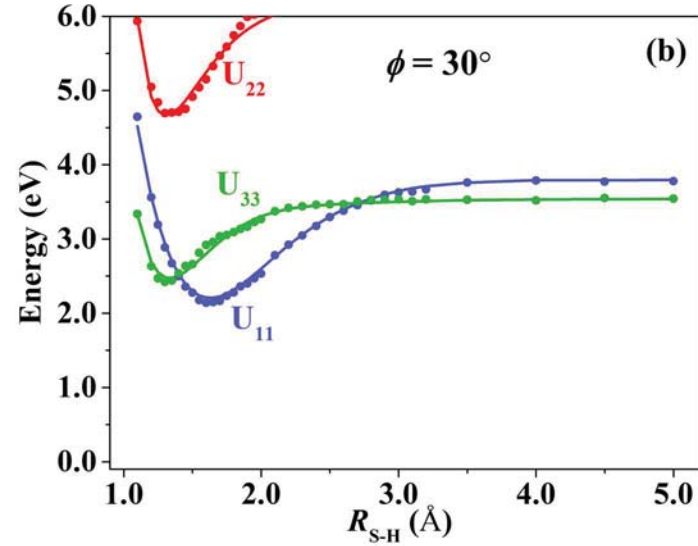
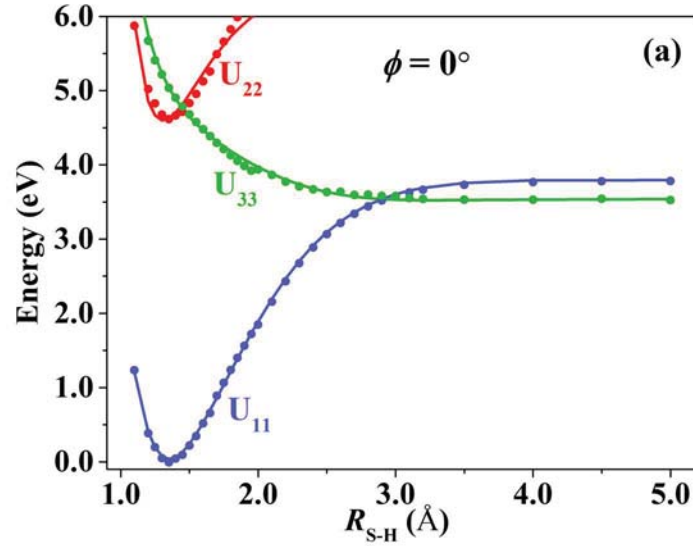
- ⁶⁴ H. Nakano, J. Chem. Phys. **99**, 7983 (1993).
- ⁶⁵ H. Nakano, Chem. Phys. Lett. **207**, 372 (1993).
- ⁶⁶ A. A. Granovsky, J. Chem. Phys. **134**, 214113 (2011).
- ⁶⁷ B. J. Lynch, Y. Zhao, and D. G. Truhlar, J. Phys. Chem. A **107**, 1384 (2003).
- ⁶⁸ M. W. Schmidt, K. K. Baldridge, J. A. Boatz, S. T. Elbert, M. S. Gordon, J. H. Jensen, S. Koseki, N. Matsunaga, K. A. Nguyen, S. Su, T. L. Windus, M. Dupuis, and J. A. Montgomery Jr, J. Comput. Chem. **14**, 1347 (1993).
- ⁶⁹ M. S. Gordon and M. W. Schmidt, *Theory and applications of computational chemistry: The First Forty Years*, edited by C. E. Dykstra, G. Frenking, K. S. Kim, and G. E. Scuseria (Elsevier, Amsterdam, 2005), p. 1167.
- ⁷⁰ P. Hohenberg and W. Kohn, Phys. Rev. **136**, 864 (1964).
- ⁷¹ W. Kohn and L. J. Sham, Phys. Rev. **140**, A1133 (1965).
- ⁷² M. E. Casida, in *Recent Advances in Density Functional Methods, Part I*, edited by D. P. Chong (World Scientific, Singapore, 1995), p. 155.
- ⁷³ H. S. Yu, X. He, S. L. Li, and D. G. Truhlar, Chem. Sci. **7**, 5032 (2016).
- ⁷⁴ A. D. Boese and N. C. Handy, J. Chem. Phys. **116**, 9559 (2002).
- ⁷⁵ A. Schäfer, C. Huber, and R. Ahlrichs, J. Chem. Phys. **100**, 5829 (1994).
- ⁷⁶ M. J. Frisch, G. W. Trucks, H. B. Schlegel, G. E. Scuseria, M. A. Robb, J. R. Cheeseman, G. Scalmani, V. Barone, B. Mennucci, G. A. Petersson, H. Nakatsuji, M. Caricato, X. Li, H. P. Hratchian, A. F. Izmaylov, J. Bloino, G. Zheng, J. L. Sonnenberg, M. Hada, M. Ehara, K. Toyota, R. Fukuda, J. Hasegawa, M. Ishida, T. Nakajima, Y. Honda, O. Kitao, H. Nakai, T. Vreven, J. A. Montgomery Jr., J. E. Peralta, F. Ogliaro, M. J. Bearpark, J. Heyd, E. N. Brothers, K. N. Kudin, V. N. Staroverov, R. Kobayashi, J. Normand, K. Raghavachari, A. P. Rendell, J. C. Burant, S. S. Iyengar, J. Tomasi, M. Cossi, N. Rega, N. J. Millam, M. Klene, J. E. Knox, J. B. Cross, V. Bakken, C. Adamo, J. Jaramillo, R. Gomperts, R. E. Stratmann, O. Yazyev, A. J. Austin, R. Cammi, C. Pomelli, J. W. Ochterski, R. L. Martin, K. Morokuma, V. G. Zakrzewski, G. A. Voth, P. Salvador, J. J. Dannenberg, S. Dapprich, A. D. Daniels, Ö. Farkas, J. B. Foresman, J. V. Ortiz, J. Cioslowski, and D. J. Fox, Gaussian 16 (Gaussian, Inc., Wallingford, CT, 2016).
- ⁷⁷ Y. P. Varshni, Rev. Mod. Phys. **29**, 664 (1957).
- ⁷⁸ P. M. Morse, Phys. Rev. **34**, 57 (1929).
- ⁷⁹ D. G. Truhlar, R. W. Olson, A. C. Jeannotte, and J. Overend, J. Am. Chem. Soc. **98**, 2373 (1976).
- ⁸⁰ S. L. Li and D. G. Truhlar, QuickFFmn 2016 (<http://comp.chem.umn.edu/abcrate/>) based on QuickFF – version 1.0.1 (<http://molmod.github.io/QuickFF>)
- ⁸¹ L. Vanduyfhuys, S. Vandenbrande, T. Verstraelen, R. Schmid, M. Waroquier, and V. Van Speybroeck, J. Comput. Chem. **36**, 1015 (2015).
- ⁸² A. W. Jasper and D. G. Truhlar, in *Conical Intersections: Theory, Computation, and Experiment*, edited by W. Domcke, D. R. Yarkony, and H. Köppel (World Scientific, Hackensack, New Jersey, 2011), p. 375.
- ⁸³ P. C. Cross, J. C. Decius, and E. B. Wilson, *Molecular Vibrations*. (McGraw-Hill, New York, 1955).

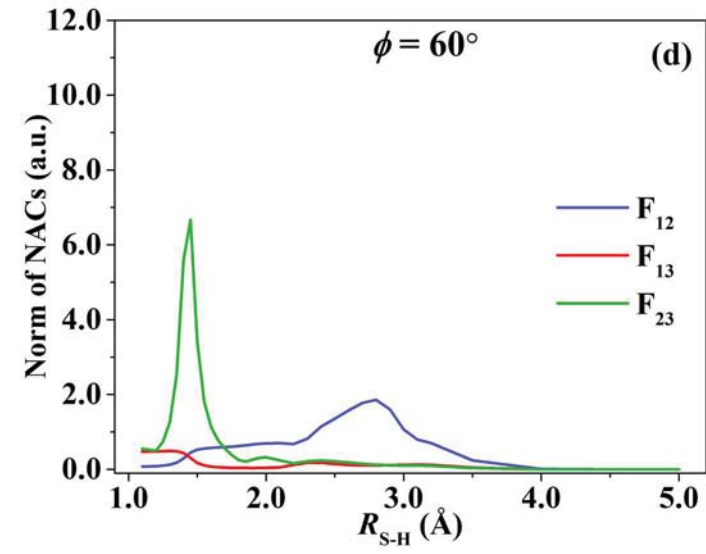
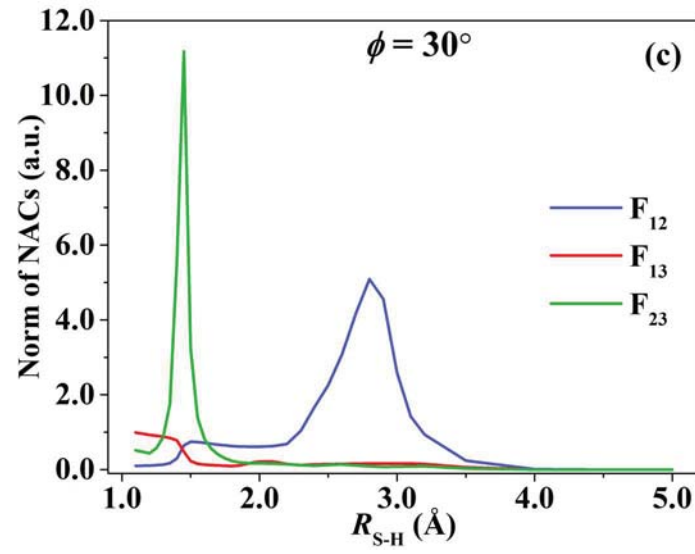
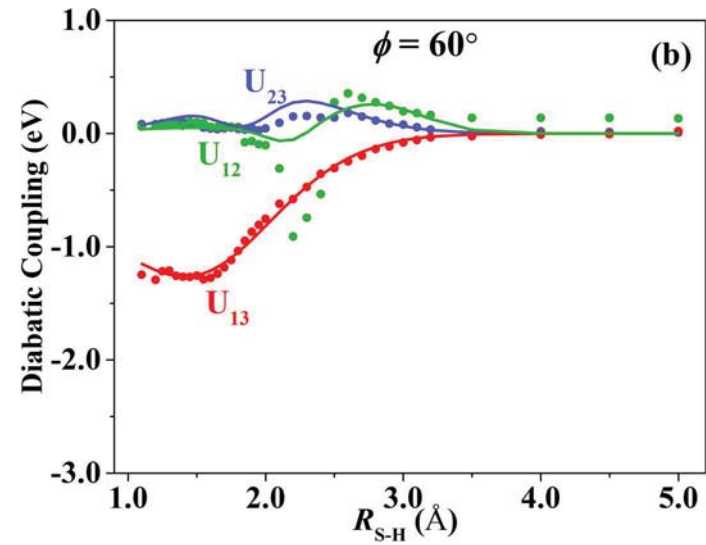
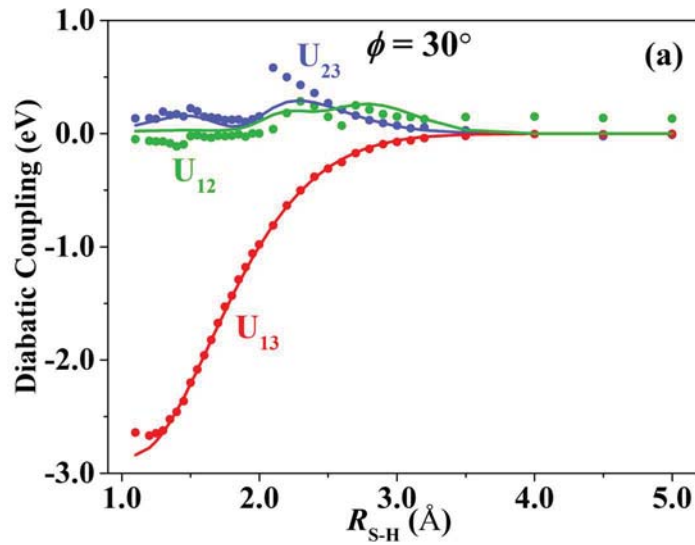
- ⁸⁴ J. Zheng, J. L. Bao, R. Meana-Pañeda, S. Zhang, B. J. Lynch, J. C. Corchado, Y.-Y. Chuang, P. L. Fast, W.-P. Hu, Y.-P. Liu, G. C. Lynch, K. A. Nguyen, C. F. Jackels, A. Fernandez Ramos, B. A. Ellingson, V. S. Melissas, J. Villà, I. Rossi, E. L. Coitiño, J. Pu, T. V. Albu, A. Ratkiewicz, R. Steckler, B. C. Garrett, A. D. Isaacson, and D. G. Truhlar, *Polyrate*-version 2017 (University of Minnesota, Minneapolis, MN, 2017).
- ⁸⁵ W. H. Press, S. A. Teukolsky, W. T. Vetterling, and B. P. Flannery, *Numerical Recipes in Fortran 77*, 2nd ed. (Cambridge University Press, 1992).
- ⁸⁶ J. Zheng, Z.-H. Li, A. W. Jasper, D. A. Bonhommeau, R. Valero, R. Meana-Pañeda, S. L. Mielke, L. Zhang, and D. G. Truhlar, ANT, version 2019, University of Minnesota, Minneapolis, 2019. <http://comp.chem.umn.edu/ant>
- ⁸⁷ K. Kowalski and P. Piecuch, *J. Chem. Phys.* **120**, 1715 (2004).
- ⁸⁸ K. Kowalski, *J. Chem. Phys.* **130**, 194110 (2009).
- ⁸⁹ T. H. Dunning Jr., *J. Chem. Phys.* **90**, 1007 (1989).
- ⁹⁰ D. E. Woon and T. H. Dunning Jr., *J. Chem. Phys.* **98**, 1358 (1993).
- ⁹¹ T. H. Dunning Jr., K. A. Peterson, and A. K. Wilson, *J. Chem. Phys.* **114**, 9244 (2001).
- ⁹² E. Papajak, J. Zheng, X. Xu, H. R. Leverentz, and D. G. Truhlar, *J. Chem. Theory Comput.* **7**, 3027 (2011).
- ⁹³ N. W. Larsen and L. Schulz, *J. Mol. Struct.* **920**, 30 (2009).
- ⁹⁴ Y. Zhao and D. G. Truhlar, *Theor. Chem. Acc.* **120**, 215 (2008).
- ⁹⁵ A. D. Becke, *Physical Review A* **38**, 3098 (1988).
- ⁹⁶ C. Lee, W. Yang, and R. G. Parr, *Phys. Rev. B* **37**, 785 (1988).
- ⁹⁷ B. Miehlich, A. Savin, H. Stoll, and H. Preuss, *Chem. Phys. Lett.* **157**, 200 (1989).
- ⁹⁸ A. D. Becke, *J. Chem. Phys.* **98**, 5648 (1993).
- ⁹⁹ F. Weigend and R. Ahlrichs, *Phys. Chem. Chem. Phys.* **7**, 3297 (2005).



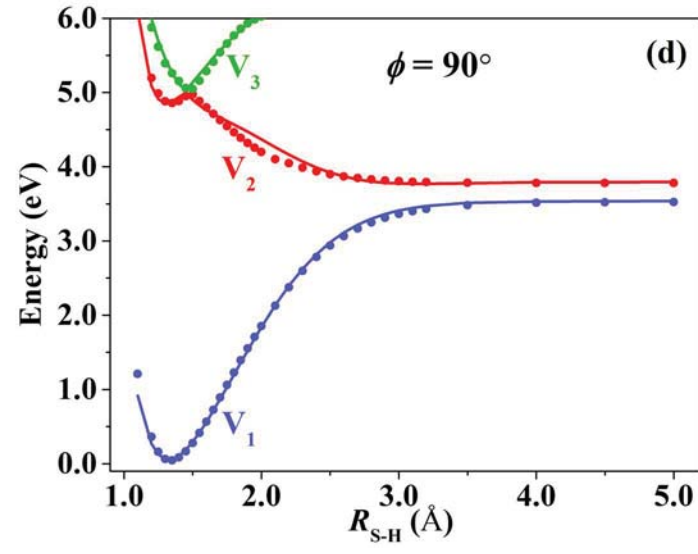
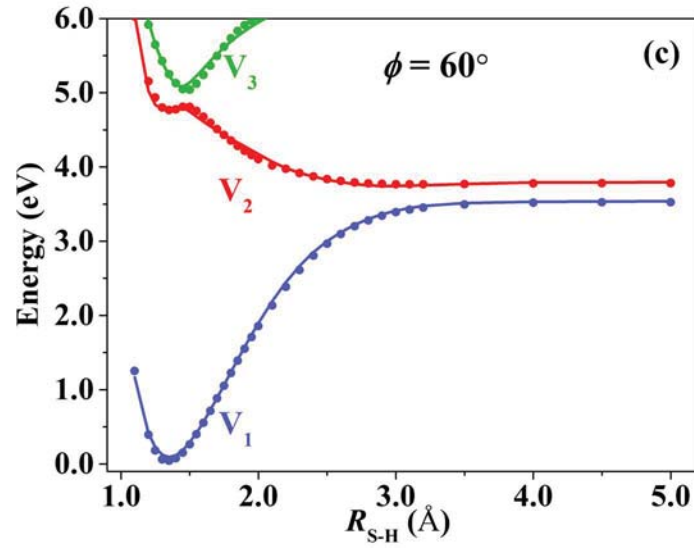
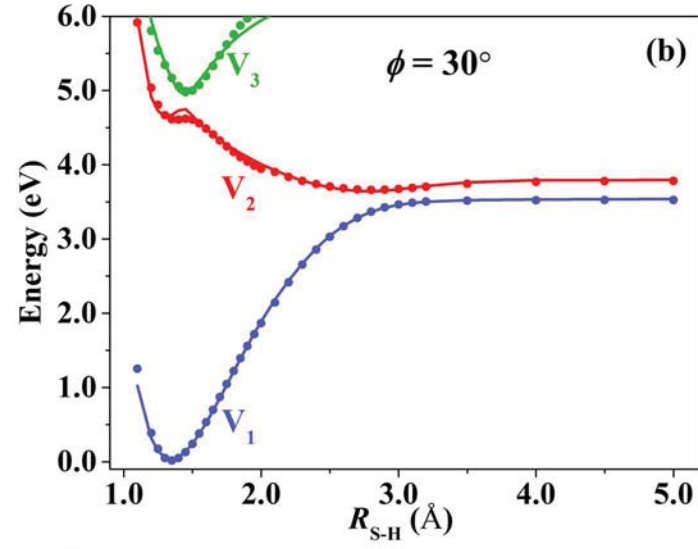
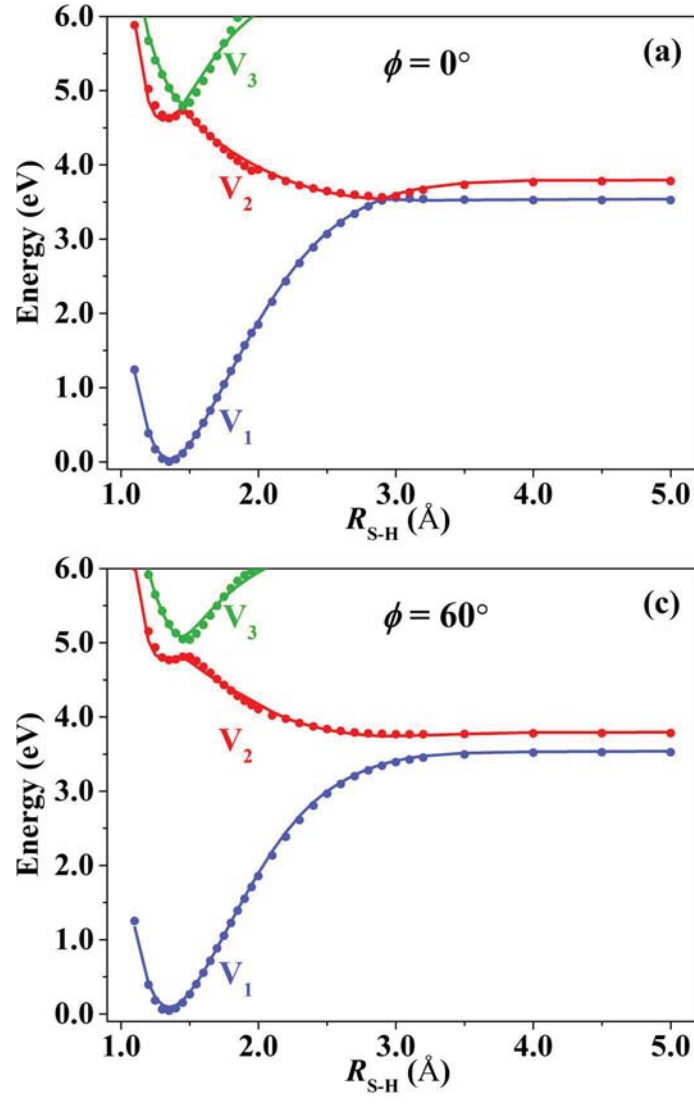


This is the author's peer reviewed, accepted manuscript. However, the online version of record will be different from this version once it has been copyedited and typeset.
PLEASE CITE THIS ARTICLE AS DOI:10.1063/1.5124870

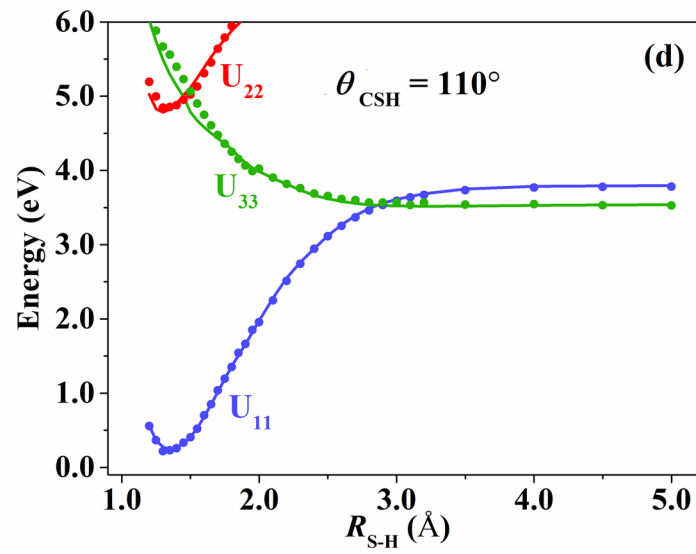
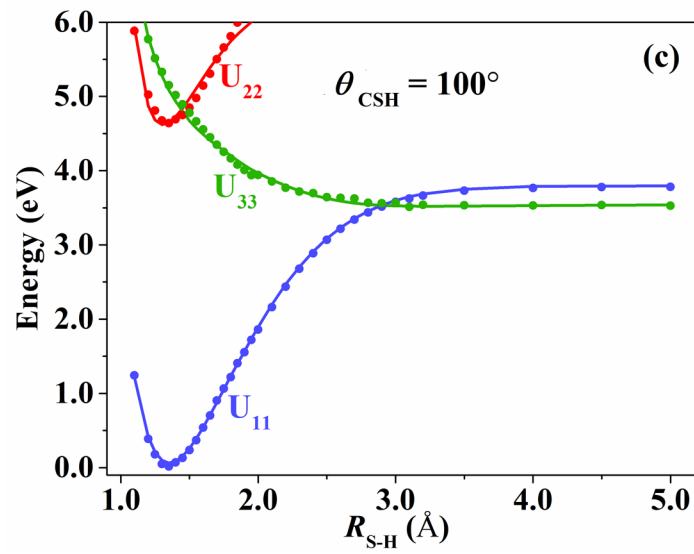
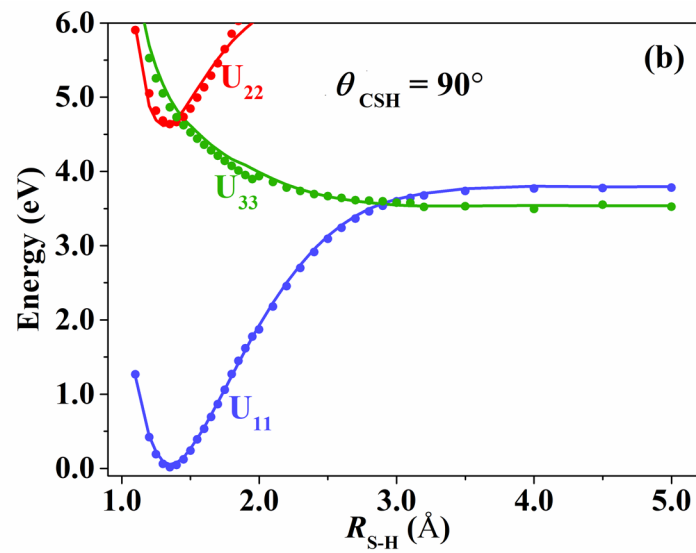
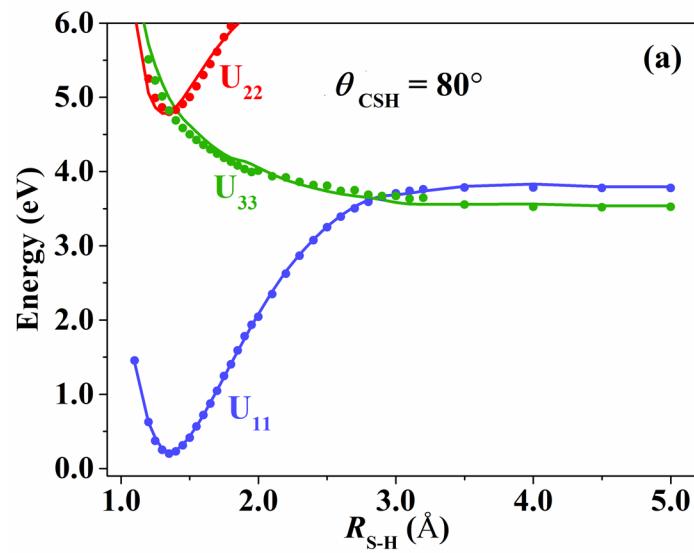




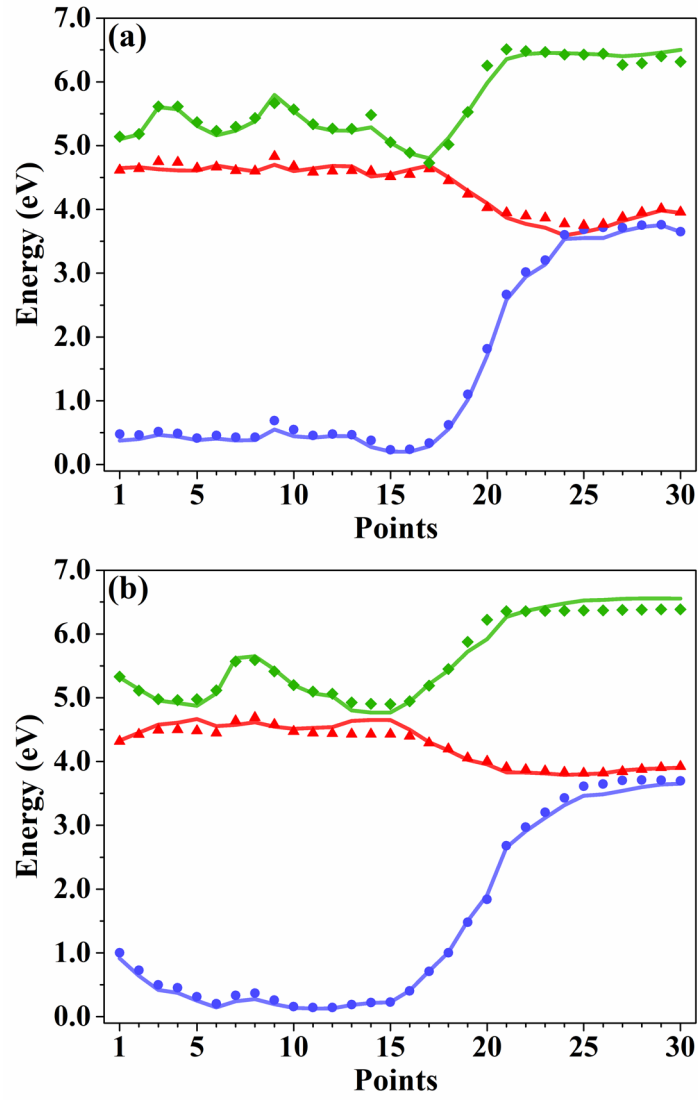
This is the author's peer reviewed, accepted manuscript. However, the online version of record will be different from this version once it has been copyedited and typeset.
PLEASE CITE THIS ARTICLE AS DOI:10.1063/1.5124870



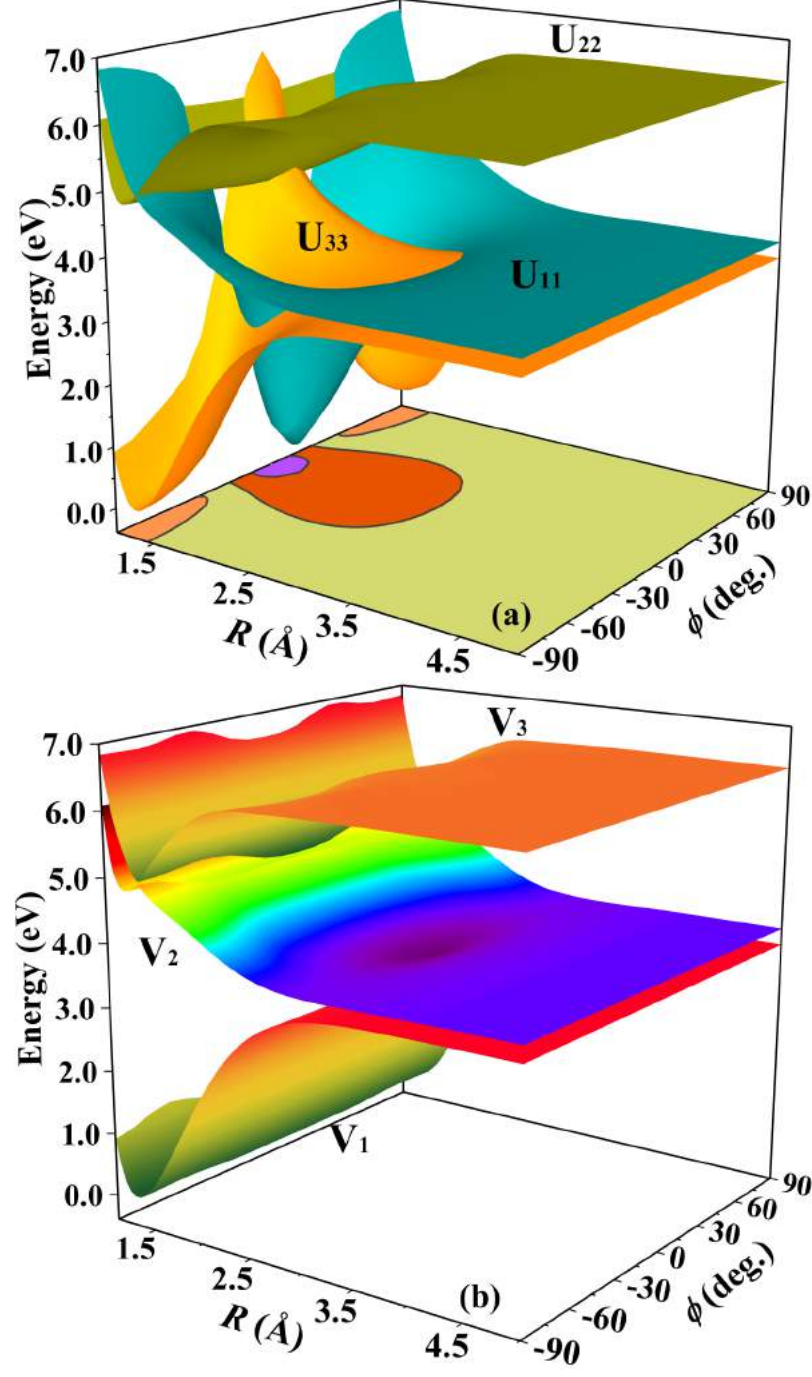
This is the author's peer reviewed, accepted manuscript. However, the online version of record will be different from this version once it has been copyedited and typeset.
PLEASE CITE THIS ARTICLE AS DOI:10.1063/1.5124870



This is the author's peer reviewed, accepted manuscript. However, the online version of record will be different from this version once it has been copyedited and typeset.
PLEASE CITE THIS ARTICLE AS DOI:10.1063/1.5124870



This is the author's peer reviewed, accepted manuscript. However, the online version of record will be different from this version once it has been copyedited and typeset.
PLEASE CITE THIS ARTICLE AS DOI:10.1063/1.5124870



This is the author's peer reviewed, accepted manuscript. However, the online version of record will be different from this version once it has been copyedited and typeset.
PLEASE CITE THIS ARTICLE AS DOI:10.1063/1.5124870

